SANDIA REPORT
SAND2003-8659
Unlimited Release
Printed December 2003

Development of Experimental Verification Techniques for Non-linear Deformation and Fracture

D. F. Bahr and N. R. Moody

Prepared by
Sandia National Laboratories
Albuquerque, New Mexico 87185 and Livermore, California 94550

Sandia is a multiprogram laboratory operated by Sandia Corporation,
a Lockheed Martin Company, for the United States Department of Energy's
National Nuclear Security Administration under Contract DE-AC04-94AL85000.

Sandia National Laboratories

Issued by Sandia National Laboratories, operated for the United States Department of Energy by Sandia Corporation.

Available to DOE and DOE contractors from
U.S. Department of Energy
Office of Scientific and Technical Information
P.O. Box 62
Oak Ridge, TN 37831

Telephone: (865)576-8401
Facsimile: (865)576-5728
E-Mail: reports@adonis.osti.gov
Online ordering: http://www.doe.gov/bridge

Available to the public from
U.S. Department of Commerce
National Technical Information Service
5285 Port Royal Rd
Springfield, VA 22161

Telephone: (800)553-6847
Facsimile: (703)605-6900
E-Mail: orders@ntis.fedworld.gov
Online order: http://www.ntis.gov/help/ordermethods.asp?loc=7-4-0#online

SAND2003-8659
Unlimited Release
Printed December 2003

Development of Experimental Verification Techniques for Non-linear Deformation and Fracture

D. F. Bahr
Mechanical and Materials Engineering
P.O. Box 642920
Washington State University
Pullman, WA 99164-2920

N. R. Moody
Microsystems and Materials Mechanics-8725
Sandia National Laboratories
P.O. Box 969 MS9404
Livermore, CA 94551-0969

Abstract

This project covers three distinct features of thin film fracture and deformation in which the current experimental technique of nanoindentation demonstrates limitations. The first feature is film fracture, which can be generated either by nanoindentation or bulge testing thin films. Examples of both tests will be shown, in particular oxide films on metallic or semiconductor substrates. Nanoindentations were made into oxide films on aluminum and titanium substrates for two cases; one where the metal was a bulk (effectively single crystal) material and the other where the metal was a 1 μm thick film grown on a silica or silicon substrate. In both cases indentation was used to produce discontinuous loading curves, which indicate film fracture after plastic deformation of the metal. The oxides on bulk metals fractures occurred at reproducible loads, and the tensile stress in the films at fracture were approximately 10 and 15 GPa for the aluminum and titanium oxides respectively. Similarly, bulge tests of piezoelectric oxide films have been carried out and demonstrate film fracture at stresses of only 100's of MPa, suggesting the importance of defects and film thickness in evaluating film strength.

The second feature of concern is film adhesion. Several qualitative and quantitative tests exist today that measure the adhesion properties of thin films. A relatively new technique that uses stressed overlayers to measure adhesion has been proposed and extensively studied. Delamination of thin films manifests itself in the form of either telephone cord or straight buckles. The buckles are used to calculate the interfacial fracture toughness of the film-substrate system. Nanoindentation can be utilized if more energy is needed to initiate buckling of the film system.

Finally, deformation in metallic systems can lead to non-linear deformation due to "bursts" of dislocation activity during nanoindentation. An experimental study to examine the structure of dislocations around indentations has been carried out to demonstrate the effectiveness in evaluating cross slip and dislocation behavior around nanoindentation impressions in bulk engineering alloys.

This page intentionally left blank

Table of Contents

List of Figures

This page intentionally left blank

Thin Film Fracture via Nanoindentation

1.1 Introduction to indentation fracture

With the increasing technological focus on the fields of microelectromechanical systems (MEMS) and microelectronic circuits, the need to characterize the material systems that comprise these devices becomes critical. Thin layers of soft metal must be sufficiently passivated and protected by hard surface layers to ensure device reliability and conductive integrity for lengthy periods of time. These protective, wear resistant coatings create either a hard-soft-hard material system, or in simpler cases consist of a hard film on a soft substrate.

Several previous studies involving the three-layer type of system are related to its ability to aid in studies of film adhesion. In this case, the hard top layer is a thin coating of a material such as tungsten or tantalum nitride that serves as a compressively stressed overlayer that triggers bucking and delamination in the underlying soft film. [1] However, placing hard films upon softer substrates does open the possibility to induce through thickness fracture in the overlying film.

Nanoindentation has been widely used to probe the mechanical response of a material by sensing penetration as low as 0.2 nm. Many studies have been carried out to understand the mechanical behavior of a coated system. For a metal coated with a hard and stiff surface film, such as Al_2O_3 on Al and TiO_2 on Ti, nanoindentation results show the presence of a yield point, which is characterized as a sudden discontinuity during loading. [2,3] The observation of plastic deformation prior to yielding excludes the possibility that the yielding is controlled by rapid dislocation nucleation and multiplication. Some experimental and numerical works have demonstrated that at yield point the surface hard film undergoes a through-thickness fracture arising from a maximum tensile stress around the contact edge.[4,5] Several analytical models, such as plate bending model and drumhead solution ,[6,7] have been proposed to describe the deformation behavior of a hard film – soft substrate system.

For this study, several model systems were selected for their ease of production and their similarities in hardness and modulus ratio to an increasingly important microelectronic material system: silicon nitride passivated copper on silicon. The main difficulties in characterizing these multilayers lie in separating their properties from each other while testing an extremely small volume of material. Both monotonic and continuous stiffness testing will be used to examine the onset of film fracture using nanoindentation.

1.2 Experimental methods for indentation fracture

Two nanoindentation systems were used in this study. The first consists of a Hysitron Triboscope, which is coupled with a Park Autoprobe scanning probe microscope for surface imaging. The indentations in this system were made using either a Berkovich diamond tip with a tip radius of approximately 1.5 μm or a 90° cube corner tip with a radius of approximately 100 nm. All indentations with the Hysitron system were made using monotonic loading. The second system was a Nanoinstruments Nanoindenter II, and used a Berkovich Accutip with a nominal root radius of 50 nm for the indenter tip. The samples were tested using the continuous stiffness method (CSM) in which an AC signal at 45 Hz is overlaid on the typical monotonic loading function. Displacement amplitudes in the CSM were varied from 3 to 9 nm to study the effect of cyclic stress accumulation on the hard oxide layers.

Two basic sets of films were chosen for this study, oxide films on bulk metallic substrates, and oxide films on thin metallic films. Oxide films on metals were grown using either anodic polarization (titanium) or thermal oxidation (aluminum). The bulk titanium sample was grade II titanium with a primarily α grain structure formed after vacuum annealing. The sample was ground to 600 grit, and electropolished in a mixture of 60% H_2SO_4, 25% HF and 15% glycerin at approximately 30 V. The anodic titanium oxide grown on bulk was tested by in-situ nanoindentation during electrochemical film growth in a solution of 0.1 M H_2SO_4. An oxide film with a film thickness of 120 nm was grown on titanium by step polarization. The detailed experimental setup can be found elsewhere.[8]

Ex-situ testing using both the Hysitron and Nanoinstruments systems was also carried out on thermal aluminum oxide on bulk aluminum, and the anodic titanium oxide on titanium films. The aluminum specimen was cut from an 1100 series aluminum ingot, ground to 1200 grit, then mechanically polished 0.05 μm. After that, the aluminum was heated in a furnace at 425^0C for 36 minutes to grow an oxide film of approximately 100nm thick . [9]

The aluminum and titanium films used in this study were grown by DC magnetron sputtering. A 1 μm titanium film was grown on a silica glass slide, while a 1 μm aluminum film was deposited on a silicon substrate. The titanium film was then anodized in 0.1M H_2SO_4 with a 6.4 V step polarization versus a Ag/AgCl electrode to obtain a 60 nm titanium dioxide layer [8]. The aluminum film was thermally oxidized[9]to obtain 60 nm of alumina. Both resulting films

were analyzed using a Digital Instruments atomic force microscope (AFM) in contact mode, and were found to have an RMS roughness on the order of 40 nm.

1.3 Results of indentation fracture

Monotonic loading of oxide films on bulk metals

The indentation of a hard film on a deforming substrate material will be approximated by the spherical loading of a hard elastic plate on a soft yielding foundation. Under contact pressure, the plate undergoes elastic deformation until brittle fracture. The substrate is displaced plastically at relatively large loads. The deformed region of the oxide film is simplified as an axisymmetric circular plate with a clamped edge. The clamped edge is defined as the outer boundary of the plastic zone, c, in the substrate. This is shown schematically in Figure 1.1 as a cross section of an indentation of a hard film on soft substrate. To first order, the size of the plastic zone developed within the substrate can be estimated by Kramer [10]

$$c = \sqrt{\frac{3P_s}{2\pi\sigma_f}} \tag{1}$$

where c is the plastic zone radius, P_s is the load carried by the substrate, and σ_f is the flow stress of the substrate.

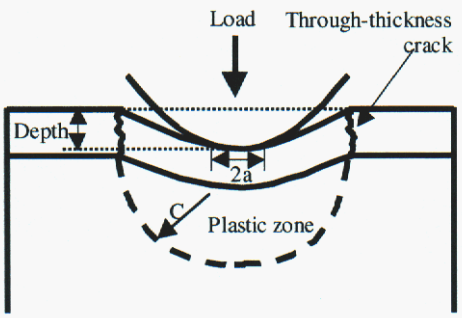

Figure 1.1. Schematic cross section of deformation profile of a hard film – soft substrate system under indentation.

The load vs. displacement for an elastic plate prior to its fracture has been described by Timeshenko,[11] and will be used to approximate a clamped elastic plate of radius c, which can then be related to the terms in equation (1) by

$$P_p = \left[\frac{2\pi^2 \sigma_f}{3} \left(\frac{16 E_f h_f^3}{12(1-\nu_f^2)} \delta + \frac{191}{648} E_f h_f \delta^3 \right) \right]^{1/2} \qquad (2)$$

where both plate bending and large-displacement stretching effects are included. P_p is the load applied to the plate, δ is the deflection depth, h_f is the plate thickness, E_f is the elastic modulus of the plate, and ν_f is the Poisson ratio of the plate.

The load and depth relationship of a monolithic material indented with a self similar indenter can be described by a power law relationship [12]

$$P = K\delta^n \qquad (3)$$

This form of the loading is somewhat empirical for this modeling, and a more complex form could be used, but in this case was chosen for ease of use. By superposition of the plate deflection solution and substrate yielding solution, the resultant relationship of the total load, P, and depth for the coated system is

$$P = K\delta^n + \left[\frac{2\pi^2 \sigma_y}{3} \left(\frac{16 E_f h_f^3}{12(1-\nu_f^2)} \delta + \frac{191}{648} E_f h_f \delta^3 \right) \right]^{1/2} \qquad (4)$$

Only two empirical constants are present in this model, K and n. Note, the first term in equation (4) is the load being carried by the substrate, while the term in brackets is being carried by the deflecting film.

Figure 1.2 shows a load - depth curve of an indentation into thermally grown aluminum oxide. The "yield point" observed allows separation between the substrate deformation and the combined film system. Assuming that the film can no longer support any pressure after the brittle fracture at yield point, nor can the remaining broken film outside the circular fracture have any functional support for the indenter as the film crack happens at a location far from the actual contact region, the loading segment after yielding can be regarded to only represent the plastic deformation of the substrate. Therefore, by fitting the portion of the loading curve after the yield

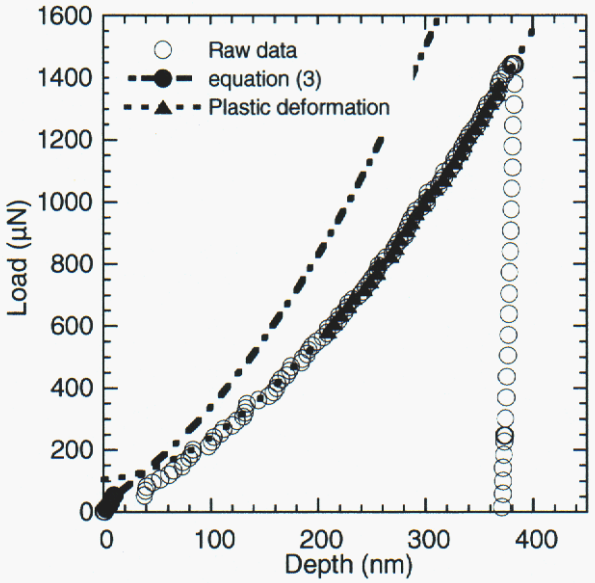

Figure 1.2. Indentation into thermally oxidized aluminum with a 100 nm thick surface oxide film. Equation (3) is demonstrated for the loading beyond the initial yield point.

point to extract K and n the substrate deformation can be described. Using these values, smaller indentations which clearly demonstrate the yield point (as shown in Figure 1.3) can be fit to equation (4), with only the flow stress of the substrate as a fitting parameter. The flow stress can be verified by making larger indentations, and checking the validity of equation (1). The fit to equation (4) for the same aluminum oxide film on aluminum is shown in Figure 1.3.

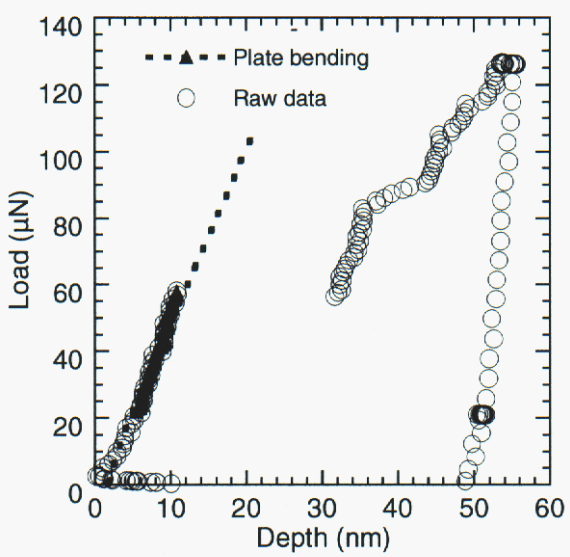

Figure 1.3. A load-depth curve for an aluminum oxide on aluminum at a lower peak load, showing the fit of the model in equation (4) with experimental data.

To verify that plastic deformation occurs prior to the yield point in these systems, indentations to loads lower than that cause an excursion in the loading curve were performed; a typical result is shown in figure 1.4. As plastic deformation does occur prior to the yield point it seems reasonable to ascribe the yield point in these experiments to film fracture, rather than dislocation nucleation.

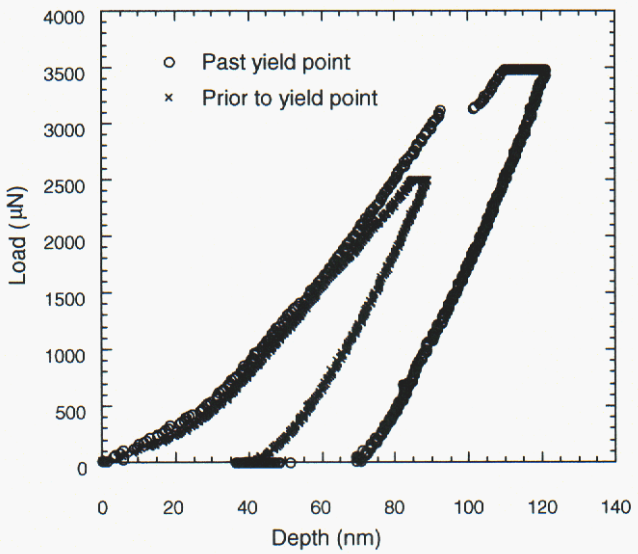

Figure 1.4. Monotonic indentations into titanium oxide on bulk titanium metal. Plastic deformation is present prior to the large yield point. Several small loading discontinuities (at approximately 100 μN) are likely due to surface roughness.

As the model fits the experimental data well, we have chosen to utilize the plate bending and stretching approach to determine the stress at fracture. Numerical simulations have shown that that the radial tensile stress around the contact edge is responsible for the film through-thickness cracking for a hard film – soft substrate composite [4]. Accordingly, the strength of the film prior to its fracture can be roughly estimated as summation of the radial stresses of both the plate bending and membrane solution [11]

$$\sigma_r = \alpha_r E_f \frac{\delta^2}{c^2} + \beta_r E_f \frac{\delta h_f}{c^2} \qquad (5)$$

where α_r and β_r are empirical constants given by [11] related to plate bending and mid-plane stretching effects, respectively. The value of α_r is 0.357 and that of β_r is 2.198. The depth and plastic zone size are evaluated at the "yield point", using the fitting of equation (4) to extract the portion of the load carried by the substrate (and hence the size of the plastic zone).

For thin oxide films grown on bulk metals, the results of the stress at film fracture are shown in Table 1. For the titanium oxide, the elastic modulus is about 300 GPa [13] , and 411GPa was used as the elastic modulus of aluminum oxide. These stresses are substantial, but are on the order of those expected for the fracture strength of a ceramic material ranges from E/100 to E/10. Previous studies [14] on aluminum oxides showed fracture strengths on bulk metal substrates grown anodically to be about an order of magnitude lower, but these were based on multiple fractures in bulk tensile specimens, and the authors suggest that their strain concentrations of a factor of three will likely be present at the film fracture sites, making the current measurements within a factor of three to these previous data.

Table 1. Applied tensile stress at fracture for indentation induced film fracture in titanium and aluminum oxides.

Material System	Oxide Film Thickness (nm)	Applied Radial Tensile Stress (GPa)
Al_2O_3/Al	100	9.8
Ti_2O/Ti	120	15

Monotonic and Cyclic Loading of oxide films on sputtered films

In the case of indentations on bulk materials, the scale of the indentation is small enough that the substrate is effectively a single crystal over the scale of the indentation, as the plastic zone radius is on the order of 100's of nm. Smaller grained films, such as those that are formed during sputtering metallic films, will not behave in a similar manner. Figure 1.5 shows the load depth curves of indentations into the titanium oxide / titanium / silica glass system using monotonic loading. In this case no excursion in the load depth curve is present. However, when tested using cyclic loading using the CSM, yield points were observed in these films. Cycling at a displacement amplitude of 9 nm on this film generated load depth curves such as the one

shown in Figure 1.6. An excursion in the load depth curve is clearly present at approximately 350 μN.

A series of indentations into the oxide films on sputtered metal films were made by varying the amplitude of displacement from 9 to 3 nm. The load at which an excursion in the load depth curve occurred was found to depend on the amplitude of the oscillation, as shown in Table 2. As the oscillation rate was 45 Hz, it is possible to determine the number of cycles (albeit at increasing mean loads) prior to the excursion. Figure 1.7 demonstrates this relationship for the titanium film. The decreasing amplitudes lead to increased numbers of cycles prior to an excursion.

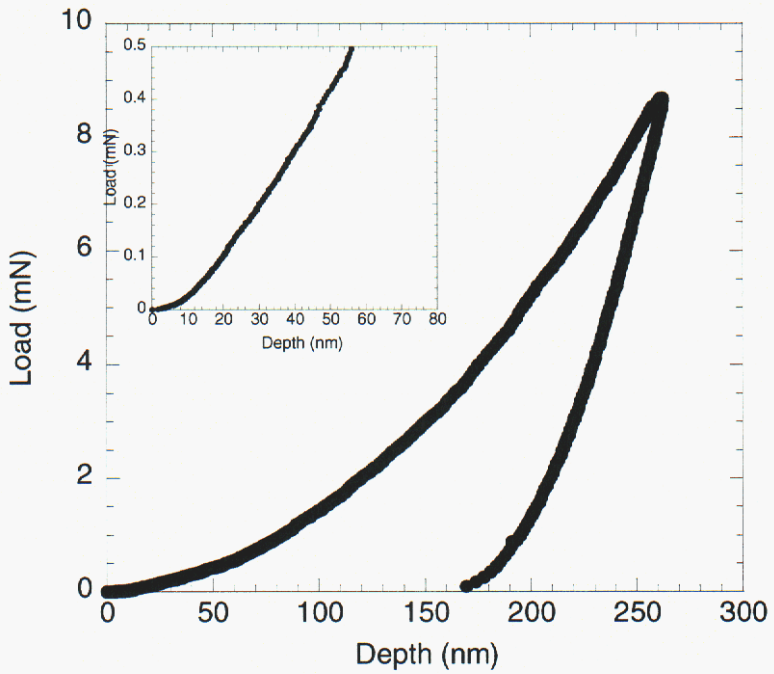

Figure 1.5. Load - depth curve of monotonically loaded sample into titanium oxide on titanium on glass. Note the inset figure, which shows no excursion in the load depth curve at low loads.

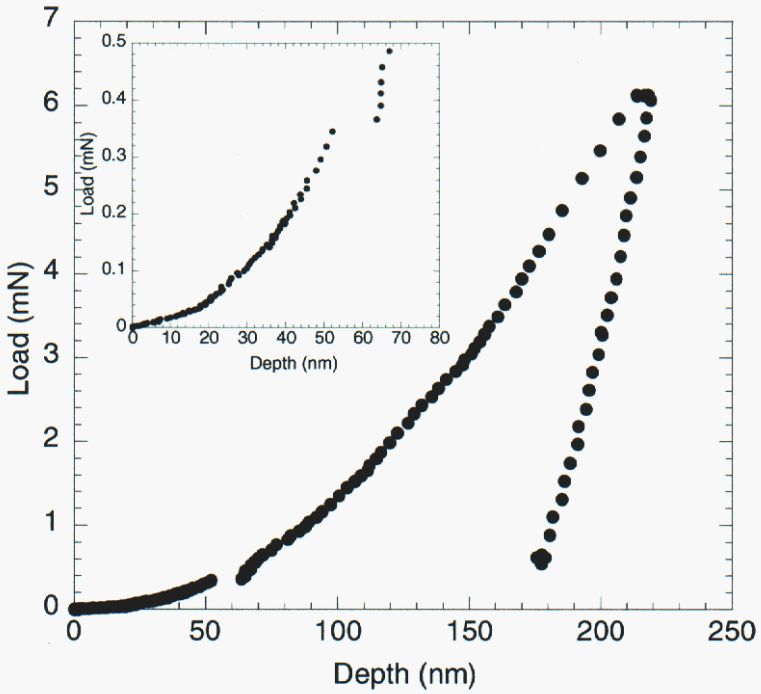

Figure 1.6. Load - depth curve of cyclically loaded sample (at 45 Hz and an amplitude of 9 nm) into titanium oxide on titanium on glass. Note the inset figure, which shows the presence of an excursion in the load depth curve at low loads.

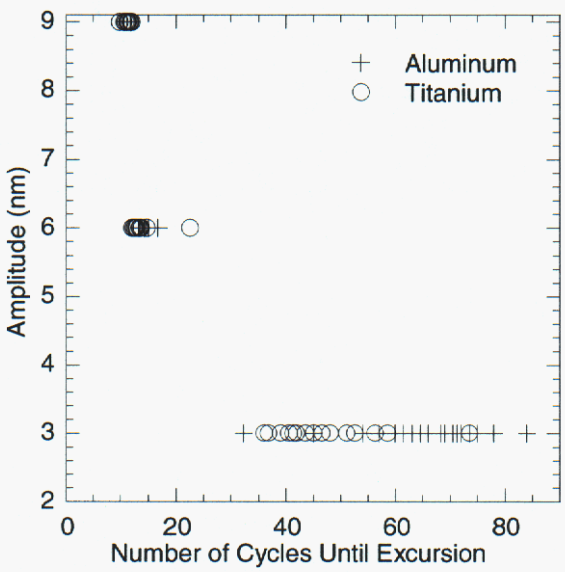

Figure 1.7. Relationship between the amplitude of cycling and the number of cycles until an excursion was observed. In all cases the cycling frequency of 45 Hz was superimposed upon a monotonic loading rate of 300 μN/s.

Table 2. Load at film fracture for the oxide / metal / glass systems tested using the CSM

Oscillation Amplitude (nm)	Ti System Load at Fracture (μN)	Al system Load at Fracture (μN)
3	309	435
6	91	97
9	74	76

An effort was made to identity the mechanism responsible for this behavior in the oxide films on sputtered films. AFM images of the indentations after the yield point, as shown in Figure 1.8, do not show any significant cracking around the indentation. This is in direct contrast to previous studies of titanium oxide on titanium, which showed cracks around an indentation at a circumference approximately equal to the expected plastic zone size [2].

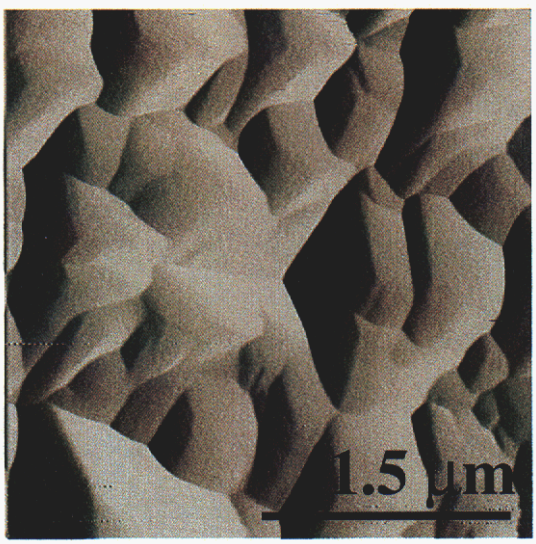

Figure 1.8. AFM image of residual impression of indentations into titanium oxide / titanium / glass.

However, there are two significant differences in the current system. First, the surface roughness of the oxide on sputtered films is significantly greater than that of the oxide films on the bulk metallic substrate. Secondly, in the titanium system the load at excursion was substantial (more than 1 mN), and so indentation to points slightly beyond the yield point can be easily found using AFM. The indentations in the cyclic loading study show excursions in the

100 μN regime. Indentations to loads just past this excursion were extremely difficult to find using AFM after removing the sample from the Nanoindenter II. The images of indentations in Figure 1.8 are after loads of 10 mN. Therefore, there are two possible explanations for the lack of observed cracks (discounting the possibility that there were never through thickness cracks in these samples as they have behaved very similar to those which have previously shown circumferential cracks around indentations). The first is that they have been obscured by the subsequent indentation, while the second is that the roughness of the surface means they have followed in the "valleys" of the rough surfaces. It seems more likely that the first option is indeed operational. The expected plastic zone size at the yield point is 400 nm (based on curve fitting data similar to figure 1.7 to extract the load carried by the substrate), which would be well inside the current visible residual impression.

The observation of loading discontinuities only occurring during cyclic loading, and in fact occurring at higher loads as the amplitude decreases (but shows no discontinuity during monotonic loading) suggest a possible mechanism for film fracture in this system. No excursions in loading during monotonic loading does not mean the film does not crack (see Bahr et al 1998[15] for AFM images of cracks in oxide films on tungsten with no loading excursions), it only means that the crack was not over driven. As indentation proceeds, if a crack is present in the oxide film it is possible to have continued crack growth without a discontinuity during loading. However, when no cracks exist in the film it seems likely that the initiation of a crack would be more difficult than the propagation of the crack. Therefore, when the critical stress required for fracture initiation is reached, the crack rapidly grows through the oxide, leading to the sudden discontinuity in the loading curve.

There are two differences in the sets of materials tested in this study (bulk and thin film substrates for oxide growth). The first is the grain size of the deforming material, and the second is the constraint of the substrate on the deformation of the film. Addressing the grain size first, it would be expected that the thin film materials are much stronger than their bulk counterparts. This would mean a significantly smaller plastic zone around the indenter, and therefore less load carried by the film deformation (and less stress in the film). The model of an elastically stretching membrane on a plastically deforming substrate breaks down as the deformation in the substrate decreases, and it could be expected many small fractures, rather than one critical fracture, would occur. However, cyclic CSM testing may increase the amount of plastic

deformation in the substrate (analogous to fatigue), which would in turn increase the load carried by the film and subsequently reach a critical value for film fracture. The second issue, the constraint of the substrate, has been addressed by other studies [16] . For instance focused ion beam cross sections of indentation demonstrate reduced deformation in the presence of a substrate [17] over a bulk material. This also would suggest the soft film between a hard film and hard substrate cannot reach a large enough plastic zone at a given film displacement to achieve a rapid fracture through the thickness of the film

1.4 Conclusions of indentation fracture

Film fracture in hard film / soft substrate systems as well as hard film / soft film / hard substrate systems has been generated via nanoindentation. The fracture strength of anodic titanium oxide on titanium is approximately 15 GPa, and the strength of a thermal aluminum oxide is approximately 10 GPa. These strengths are for a thin film on a bulk metal, and modeled as the elastic deformation of a hard film on a plastically deforming substrate. However, when similar oxides are grown on sputtered metallic films on hard substrates, the differences in metal grain size and the constraint of the substrate change the deformation pattern which allows for hard film / soft substrate film fracture. In the multilayer film systems, monotonic loading did not generate an isolated rapid fracture event. Instead, cyclic loading using the CSM method caused film fracture. This is suggested to be caused by increased plasticity in the metal film with the cycling of the indentation, allowing the conditions of a stretched and bent membrane over a plastically deforming substrate to be achieved. Future use of nanoindentation for film fracture methods in multilayer systems will require underlying films which are able to deform significantly while the hard overlayer is elastically stretched for the model presented here to be appropriate to calculate film fracture stresses.

1.5 References

1. Bahr, D.F., Kramer, D.E. and Gerberich,W.W., Non-linearDeformation Mechanisms During Indentation, *Acta Materiala*, 46, (1998) 3605-3617.

2 . Pang, M. and Bahr, D. F., Thin Film Fracture During Nanoindnetation Of A Titanium Oxide Film – Titanium System *Journal of Materials Research*, 16, (2001) 2634-2643.

3 . Chechenin, N. G., Bottiger, J. and Krog, J. P., Nanoindentation of Amourphous Aluminum Oxide Films II. Critical Parameters for the Breakthrough and a Membrane Effect in Thin Hard Films on Soft Substrates, Thin Solid Films, 261, (1995) 228-235.

4. Weppelman, E. and Swain, M. V., Investigation of the stresses and stress intensity factors responsible for fracture of thin protective films during ultra-micro indentation tests with spherical indenters Thin Solid Films, 286 (1996) 111-121.

5 . Page, T.F. and Hainsworth, S.V., Using nanoindentation techniques for the characterization of coated systems: a critique Surface and Coating Technology, 61 (1993) 201-208.

6 . McGurk, M.R., Chandler, H.W., Twigg, P.C., Page, T.F., Modelling the hardness response of coated systems: the plate bending approach, Surface and Coating Technology, 68/69, (1994) 576-581.

7 . Gerberich, W. W., Strojny, A., Yoder, K., and Cheng, L-S, Hard protective overlayers on viscoelastic-plastic substrates Journal of Materials Research, 14, (1999) 2210-2218.

8 . Pang, M., Eakins, D.P., Norton, M.G. and Bahr, D.F., Structural and Mechanical Characteristics of Anodic Oxide Films on Titanium *Corrosion*, 57 (2001) 523-531.

9 . Alymore, D.W., Gregg, S.J. and Jepson,W.B., *Journal of the Institute of Metals*, 88, (1959) 205-208

10 . Kramer, D., Huang, H., Kriese, M., Robach, J., Nelson, J., Wright, A., Bahr, D. and Gerberich, W. W., Yield Strength Predictions From the Plastic Zone Around Nanocontacts, *Acta Materialia*, 47 (1998) 333-343.

11 . Timoshenko, S. and Woinowshy-krieger, S., Theory of Plates and Shells, McGraw-Hill, 1959.

12 . Hainsworth, S.V., Chandler,H.W., and Page, T. F., Analysis of nanoindentation load-displacement loading curves , *Journal of Materials Research*, 8, (1996) 1987-1995.

13 . Barsoum, Michel, Fundamentals of Ceramics, McGraw-Hill, 1997.

14 . Grosskreutz, J.C., Mechanical Properties of Metal Oxide Films, *Journal of the Electrochemical Society*, 116 (1969) 1232-1237.

15 . Bahr, D.F., Hoehn, J.W., Moody, N.R., and Gerberich, W.W., Adhesion and acoustic emission analysis of failures in nitride films with a metal interlayer, *Acta Materialia*, 45 (1997) 5163-5175.

16 . Kramer, D.E., Volinsky, A.A., Moody, N.R., and Gerberich,W.W., Substrate effects on indentation plastic zone development in thin soft films, *Journal of Materials Research*, 16 (2001) 3150-3157.

17 . Tsui, T.Y. and Pharr, G.M., Substrate effects on nanoindentation mechanical property measurement of soft films on hard substrates, *Journal of Materials Research*, 14 (1999) 292-301.

Thin Film Adhesion

2.1 Adhesion of thin films

The adhesion of thin films is an important property for performance and reliability of many thin film microelectronics. Failure of these devices can occur if the thin films delaminate from one another. In order to ensure that the device will not fail, it is important to know the amount of energy it takes for the films to delaminate, or the interfacial fracture toughness ($\Gamma(\Psi)$). This value, also called the practical work of adhesion, takes into account the thermodynamic work of adhesion between the materials at the interface and the energy dissipated by the film and substrate [1]. The energy dissipated includes inelastic contributions from ligament bridging, plasticity at the interfacial crack tip and friction between the tip and film [2].

The practical work of adhesion can be determined qualitatively or quantitatively depending on the test method [3]. Different methods to calculate the adhesion energy, or interfacial fracture toughness, have been developed. Some methods use a microprobe to scratch [4-7] or indent [8-12] the surface. Scratch testing continuously measures the force and displacement of the microprobe, generally a diamond tip, to generate an interfacial crack and spalling. Nanoindentation can be used to either induce spontaneous buckling of the film or to create indentation blisters, depending on the residual stress of the film. Four point bend and sandwich specimens test a macroscopic sample that incorporates a thin film into its structure [13]. The thin film is usually incorporated using diffusion bonding which can alter the film's microstructure and interface properties, and as a result do not test the as-deposited state of films. Another adhesion test method is the stressed overlayer, or superlayer, method [14-15]. The stressed overlayer method uses a highly compressively stressed film of a refractory metal that is deposited over a film system of interest to drive film delamination. If the overlayer has enough strain energy then it can cause spontaneous buckling to occur in the underlying film system in the form of telephone cord or straight buckles. If the stressed overlayer does not have enough energy to cause spontaneous buckling then nanoindentation can be used to add additional elastic strain energy and induce buckling of the films in the form of indentation blisters. The dimensions of the buckles and blisters are used in mechanics based models to calculated adhesion energy [11, 16]. All of these techniques have been used to successfully calculate the interfacial fracture toughness of several film systems [6-15, 17-18].

There are ways to increase the adhesion energy of thin films. Many researchers have studied the effects of annealing films, such as copper, to increase the interfacial fracture toughness [19-20]. Others have examined the effect surface roughness can have on the interfacial fracture toughness of a system [21]. Tymiak et al. [22] studied the role of plasticity as a possible mechanism for increasing the interfacial fracture toughness and others [23-25] have studied interface chemistry effects. Finally, the addition of thin (less than 50 nm) layers to promote adhesion [17, 26] has been demonstrated. Typical adhesion layer materials include copper, chromium, and titanium. These metals exhibit high oxidation activities, which tend to promote adhesion to oxide substrates.

As mentioned before, thin films are being used in microelectronic devices as well as in MEMS (micro-electrical mechanical systems) and NEMS (nano-electrical mechanical systems) devices. Platinum is of interest because it is commonly used as the bottom electrode material for piezoelectric MEMS devices [27-29] and is imperative that it has high adhesion with the substrate (SiO_2). Platinum has trouble adhering well to any substrate and therefore an interlayer of titanium or zirconium is often used to promote adhesion [29]. In order to extract the interfacial fracture toughness of the Pt-SiO_2 interface a tungsten stressed overlayer and a tungsten stressed overlayer coupled with nanoindenation have been utilized and the test methods compared to a single platinum film. Finally, the effect of a titanium interlayer on the adhesion has been examined using a tungsten stressed overlayer and nanoindentation only, as the additional elastic strains from the indentation process were required to cause delamination at the Ti-SiO_2 interface.

2.2 Adhesion testing methods and materials

Platinum films and platinum/titanium films were deposited on SiO_2 (glass microscope slides) using DC magnetron sputtering. A 300 nm stressed overlayer of tungsten was deposited onto one 280 nm platinum film also using DC magnetron sputtering. The stress in the first tungsten overlayer was measured using wafer curvature and Stoney's equation, and had a compressive stress of 30 MPa. A second tungsten overlayer was deposited onto the platinum/titanium film (175 nm/12 nm) with a compressive residual stress of 2.1 GPa and a thickness of 450 nm. Table I summarizes the samples tested. An array of indentations were made into the W/Pt film system and the W/Pt/Ti film system with loads varying between 25 mN

to 550 mN using a NanoInstruments Nanoindenter II with a 1 μm tip radius, 90° degree conical diamond tip. An atomic force microscope (AFM) was used to image and measure the buckles and blisters. A minimum of 15 buckles were measured on each sample. The dimensions of the buckles and blisters were used to calculate the interfacial fracture toughness using the adhesion mechanics of Hutchinson and Suo [16].

Table I: Summary of Samples Tested

	Stressed Overlayer & sputtering pressure	Base Film & sputtering pressure	Interlayer & sputtering pressure	Substrate	Adhesion Test Method
Pt/SiO_2	None	Pt 8mTorr	None	SiO_2	Spontaneous buckles
$W/Pt/SiO_2$	W 2.9 mTorr	Pt 14 mTorr	None	SiO_2	Spontaneous buckles
$W/Pt/SiO_2$	W 2.9 mTorr	Pt 14 mTorr	None	SiO_2	Indentation induced blisters
$W/Pt/Ti/SiO_2$	W 3.6 mTorr	Pt 11 mTorr	Ti 1.6 mTorr	SiO_2	Indentation induced blisters

2.3 Adhesion results and discussion

One Dimensional Buckles

One platinum film spontaneously buckled in the form of telephone cord and straight buckles soon after deposition was complete, as shown in Figure 2.1. The tungsten/platinum film formed spontaneous telephone cord buckles in one region after the stressed overlayer was deposited as illustrated in Figure 2.2.

Figure 2.1: Straight and telephone cord buckles formed on the platinum film.

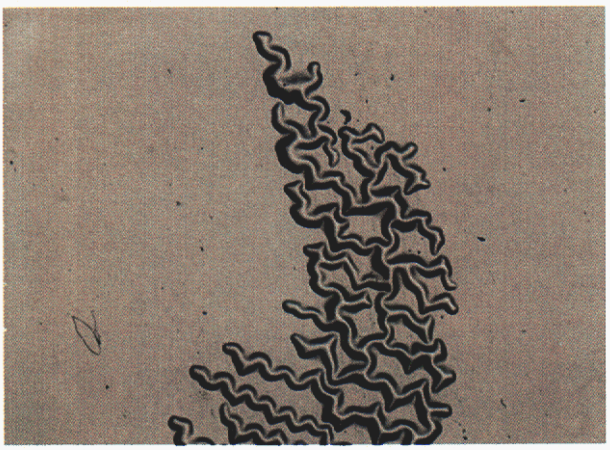

Figure 2.2: Spontaneous buckles formed on the platinum film with the addition of a tungsten stressed overlayer in the form of telephone cord buckles.

These buckles can be modeled as a one-dimensional buckle if the midpoint position of the telephone cord is chosen as the region to measure (Figure 2.3). The dimensions of the spontaneous buckles were measured with AFM and used to calculate the stresses that arose during the buckling process. The critical buckling stress, σ_b, and the driving stress, σ_d, of the film [16] depend on the film thickness, h, and the radius of the buckle, b, and the height of the buckle, δ (Figure 2.4). In this model the critical buckling stress, σ_b, and driving stress, σ_d, are given by

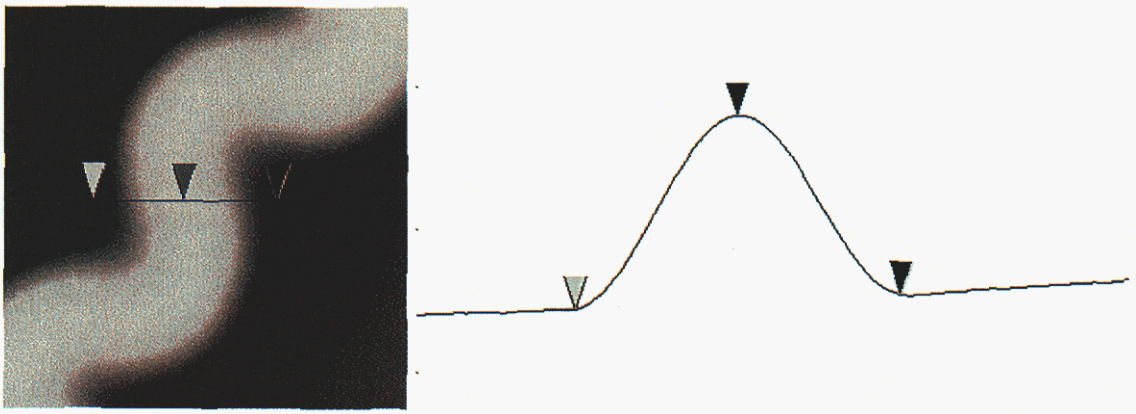

Figure 2.3: Example of how spontaneous telephone cord buckles were measured.

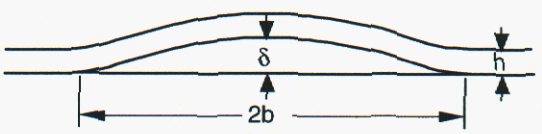

Figure 2.4: Schematic of the cross-section of a spontaneous buckle.

$$\sigma_b = \frac{\mu^2 E}{12(1-\nu^2)}\left(\frac{h}{b}\right)^2 \qquad (1)$$

$$\sigma_d = \sigma_b\left[c_1\left(\frac{\delta}{h}\right)^2 + 1\right] \qquad (2)$$

where μ^2 equals π^2 and c_1 is 3/4 [16]. The critical buckling stress is the stress needed for film buckling to occur while the driving stress aids in the propagation of the delamination. The mixed mode interfacial fracture toughness, $\Gamma(\Psi)$ for spontaneous buckles is calculated using

$$\Gamma(\Psi) = \left[\frac{(1-\bar{\nu}^2)h}{2\bar{E}}\right](\sigma_d - \sigma_b)(\sigma_d + 3\sigma_b) \qquad . \qquad (3)$$

The $\Gamma(\Psi)$ for the Pt film and the W/Pt film are 1.7 and 2.1 J/m^2, respectively. The phase angle of loading, Ψ, is found using

$$\Psi = \tan^{-1}\left[\frac{4\cos\omega + \sqrt{3}\xi\sin\omega}{-4\sin\omega + \sqrt{3}\xi\cos\omega}\right] \qquad (4)$$

where ω is 52.1° [30] and $\xi=\delta/h$. Equation 4 is valid for all σ_d/σ_b ratios less than 7.6. The value for ω was obtained through numerical means by Suo and Hutchinson [30] as well as Thouless, Evans, Ashby, and Hutchinson [31]. After σ_d/σ_b reaches 7.6 in the one dimensional buckle the phase angle is approximately equal to -90° due to the large amount of shear forces present. The phase angle of loading can also be determined graphically using an analysis by Hutchinson and Suo and uses the stress ratio (σ_d/σ_b) of the film [16]. Due to the large amount of shear forces present and the high stress ratio, the platinum film had phase angle of loading of -90°. The phase angle of the W/Pt film system was calculated to be -85° when the stressed overlayer buckles were used. A summary of the results can be found in Table II.

Table II: Summary of Interfacial Fracture Toughness values for all samples

Interface & Method	$\Gamma(\Psi)$ (J/m^2)	Ψ	Γ_I (J/m^2)
Pt/SiO_2 Buckles	1.7	-90	0.4
$W/Pt/SiO_2$ SOL Buckles	2.1	-85	0.6
$W/Pt/SiO_2$ SOL Blisters	0.4	-57.5	0.2
$W/Pt/Ti/SiO_2$ SOL Blisters	2.0	-64.1	1.0

Axisymetric Indentation Induced Delamination

All the blisters that formed on the W/Pt film with nanoindentation were relatively circular in shape and the indents at the higher loads (greater than 200 mN) almost initiated spontaneous buckling, as seen in Figure 2.5. Similarly, the same type of blisters can be observed for the W/Pt/Ti indentation experiments in Figure 6. AFM of delaminated regions show that the Pt-SiO_2 interface and the Ti-SiO_2 interface are location of the fracture. This can be seen in Figure 7b, where a cross-section across the delaminated region shows platinum and tungsten steps equal to the thicknesses of these films.

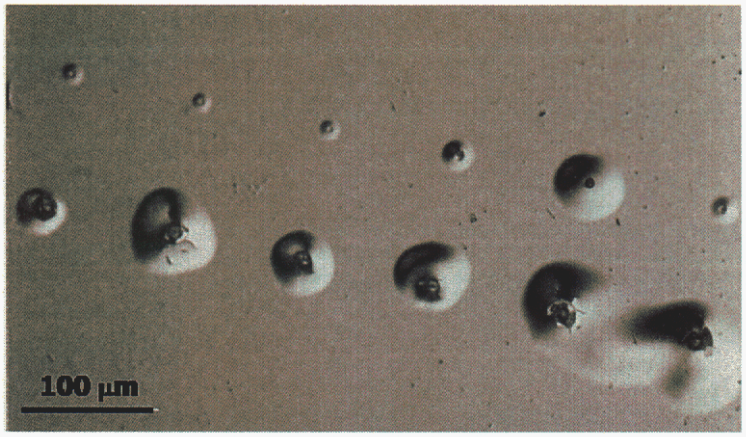

Figure 2.5: Regular shaped blisters formed on the W/Pt film. The higher indent loads formed incipient telephone cord buckles.

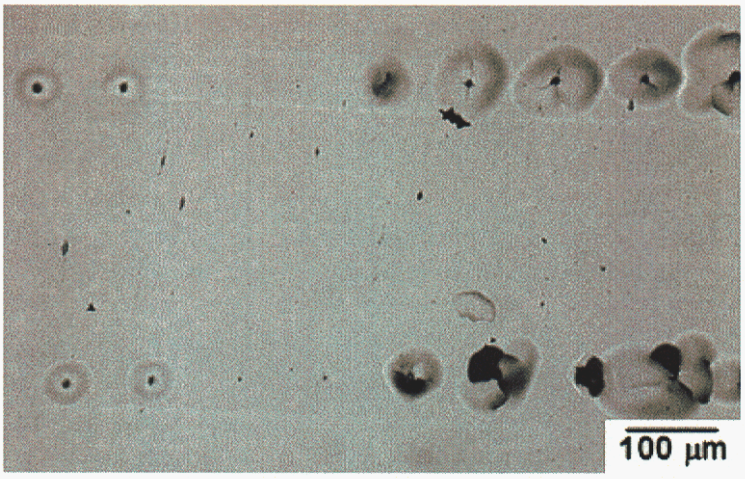

Figure 6: Large blisters formed on the W/Pt/Ti film when indentation experiments were performed. At higher loads cracking of the film around the indent occurred along with complete film delamination.

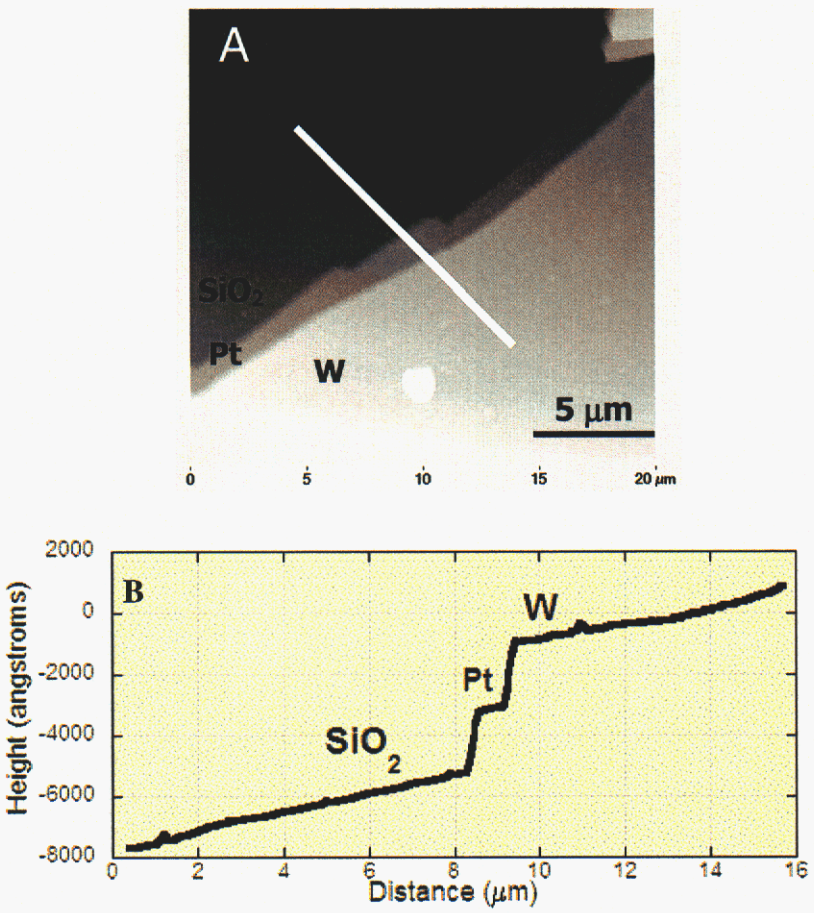

Figure 2.7: a) AFM image of edge of delaminated region of the W/Pt/SiO_2 film system. b) Cross-section of AFM height image in (a). The step heights correspond to the thicknesses of the tungsten and platinum films.

The load-depth curves from the indentation experiments were examined to determine the volume of the indent and to aid in the modeling of the adhesion mechanics. It must be noted that all of the indents went through the film thickness and well into the substrate for W/Pt film and W/Pt/Ti film. As such, the volume of the indent that contributes to delamination is more difficult to determine once the indent has gone through the film thickness. Kriese et al. [8] has commented that the calculation of the volume of the indent using the tip geometry and the inelastic penetration depth is a reasonable procedure but can be a large source of error. For this reason the indentation blisters are modeled as a circular blisters using the Hutchinson and Suo model [16] and the volume of the film displaced by the indenter tip is ignored. Instead, by

measuring the height and dimensions of the blister the effective driving stress (the stress which caused that shape blister) can be determined. Excursions, or pop-in events, which would be indicative of delamination at the interface followed by through thickness film fracture, did not occur at any time during the indentation tests for the W/Pt film but did occur for the W/Pt/Ti film during the loading of the indenter, as shown in Figure 2.8. Therefore, W/Pt film is modeled after an unpinned circular blister due to the absence of excursions and the W/Pt/Ti film is modeled as a pinned circular blister because of the excursion present in the load versus displacement curve. An unpinned blister forms after the indenter tip has been removed and a pinned blister forms while the indenter tip is still in contact with the film (Figure 2.9).

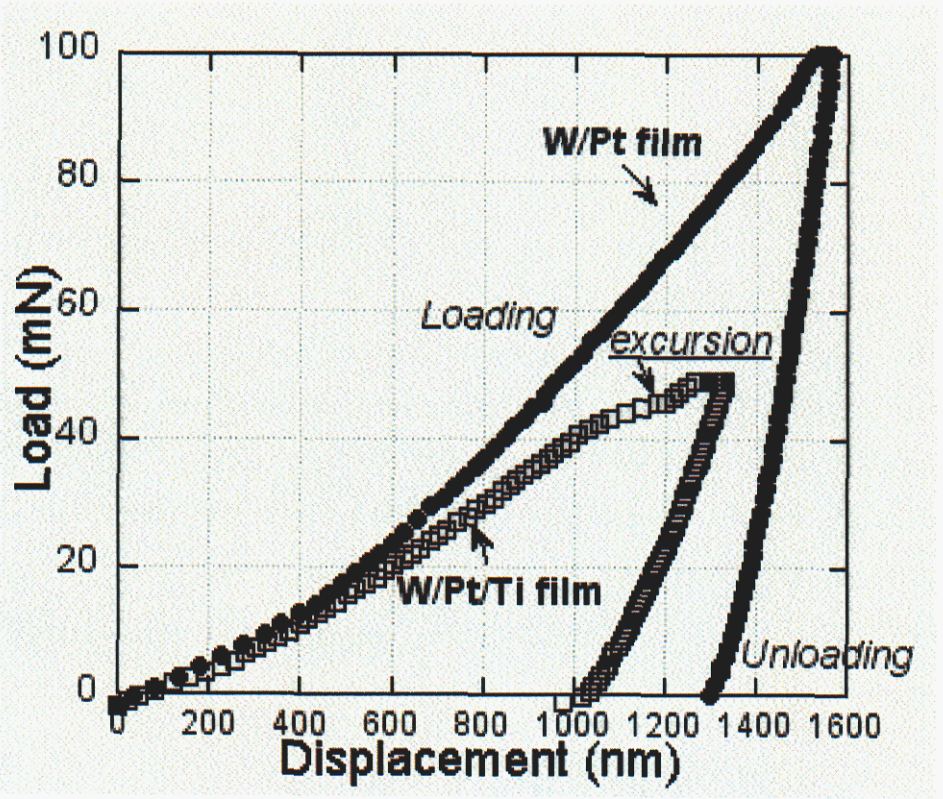

Figure 2.8: Load-depth curves for the W/Pt and W/Pt/Ti film systems. The W/Pt/Ti system has an excursion during the loading that indicates interfacial fracture during loading.

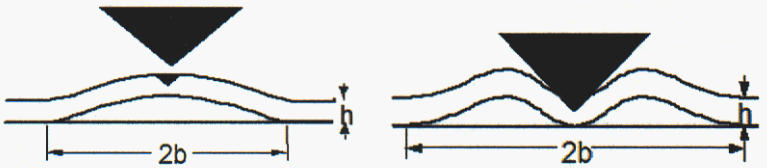

Figure 2.9: Schematic of an unpinned circular blister (left) and a pinned circular blister (right).

The critical buckling stress and driving stress for indentation blisters were calculated using equations 1 and 2 where, but now μ^2 is 14.68 for an unpinned blister and 42.67 if the blister is pinned in the center (Figure 2.9) and $c_1 = 0.2473(1+\nu)+0.2231(1-\nu^2)$. $\Gamma(\Psi)$ can be calculated using

$$\Gamma(\Psi) = c_2\left[1-\left(\frac{\sigma_b}{\sigma_d}\right)^2\right]\frac{(1-\nu)h\sigma_d}{E} \qquad (5)$$

where $c_2=[1+0.9021(1-\nu)]^{-1}$. The largest circular shaped blisters without radial cracks on the W/Pt and W/Pt/Ti films where chosen to calculate the interfacial fracture toughness of these samples, as a previous study showed a size dependence of indentation blisters on the calculation of interfacial fracture toughness [32]. Blisters of this size were large enough so that there was no interaction from the indenter tip or added plasticity effects. The interfacial fracture toughness, $\Gamma(\Psi)$, was calculated to be 0.4 J/m^2 for the W/Pt film and 2.0 J/m^2 for the W/Pt/Ti film system. All of the calculated values correlate well with one another, and are given in Table II.

The term Ψ is again the phase angle of loading and is calculated using ω=52.1° and $\xi=\delta/h$ in [16]

$$\tan\Psi = \frac{\cos\omega + 0.2486(1+\nu)\xi\sin\omega}{-\sin\omega + 0.2486(1+\nu)\xi\cos\omega} \qquad (6)$$

Equation 6 is valid for stress ratios (σ_d/σ_b) less than two. When the stress ratio is greater than two, then

$$\tan\Psi = \frac{\cos\omega + \dfrac{h\Delta N}{\sqrt{12}M}\sin\omega}{-\sin\omega + \dfrac{h\Delta N}{\sqrt{12}M}\cos\omega} \qquad (7)$$

where ω is 52.1° and $\frac{h\Delta N}{\sqrt{12}M}$,taken from Figure 64b from Hutchinson and Suo [16], must be used to calculate the phase angle of loading. This combination allows for the determination the phase angle for any elastic mismatch. The phase angles of loading were calculated to be -54.5° for the W/Pt film system and -64.1° for the W/Pt/Ti film system when indention blisters and the stressed overlayers were used.

The practical work of adhesion also depends on the mode mixity, or phase angle of loading, Ψ. When the phase angle of loading is 0^{o}, then the fracture toughness is determined entirely from normal forces and is called the mode I fracture toughness. When the crack is under of pure shear, the phase angle of loading is $\pm 90^{o}$ resulting in mode II fracture. Knowing Ψ and the $\Gamma(\Psi)$ allows for the approximation of the mode I fracture toughness (Γ_I) using

$$\Gamma_I = \Gamma(\Psi)/\left[1+\tan^2\{(1-\lambda)\Psi\}\right] \tag{8}$$

where λ is a material parameter close to 0.3. The mode I fracture toughness is thought of as the practical work of adhesion because it takes into account not only the true work of adhesion but also the energy dissipated by the film and substrate. It also helps define the fundamental fracture process. The value obtained using equation (8) is an empirical relationship derived from fracture mechanics [16].

Using the calculated phase angles of loading and equation (8), the opening mode interfacial fracture toughness was determined from indentation to be 0.2 J/m^2 for the platinum interface and 1.0 J/m^2 for the titanium interface. This result indicates that titanium increases the interfacial fracture toughness of Pt to SiO_2 by a factor of approximately five.

The standard deviations of the interfacial fracture toughness values are not reported in Table II due to the large difference in the number of measurements taken for each film system. Spontaneous buckles are more prevalent and therefore more buckles can be measured. On the other hand, only a few indentation blisters achieve the ideal size and shape that can be used in the adhesion models. For example, in the case of the W/Pt/Ti film system, only four of 24 indents created an ideal indentation blister and were used in the analysis, whereas over 15 buckles from the platinum and W/Pt films were used for the one dimensional cases. The total range of $\Gamma(\Psi)$ calculated for the W/Pt indents was 0.33 to 0.47 J/m^2 and for the W/Pt/Ti indents was 1.7 to 2.4 J/m^2.

The results for the spontaneous buckles and indentation blisters compared well with the analytical models of Hutchinson and Suo [16] and Moon et al [33] as shown in Figure 2.10. The phase angle of loading is plotted against the stress ratio for the spontaneous platinum buckles induced by the stressed overlayer and the indentation blisters of the W/Pt and W/Pt/Ti films. The experimental values correspond very well with the model, indicating that the stressed overlayer method and the stressed overlayer method coupled with nanoindentation are valid techniques to use to quantitatively determine the interfacial fracture toughness of thin film systems. Indentation blisters generally give a lower bound of the interfacial fracture toughness and the spontaneous buckles generally give an upper bound.

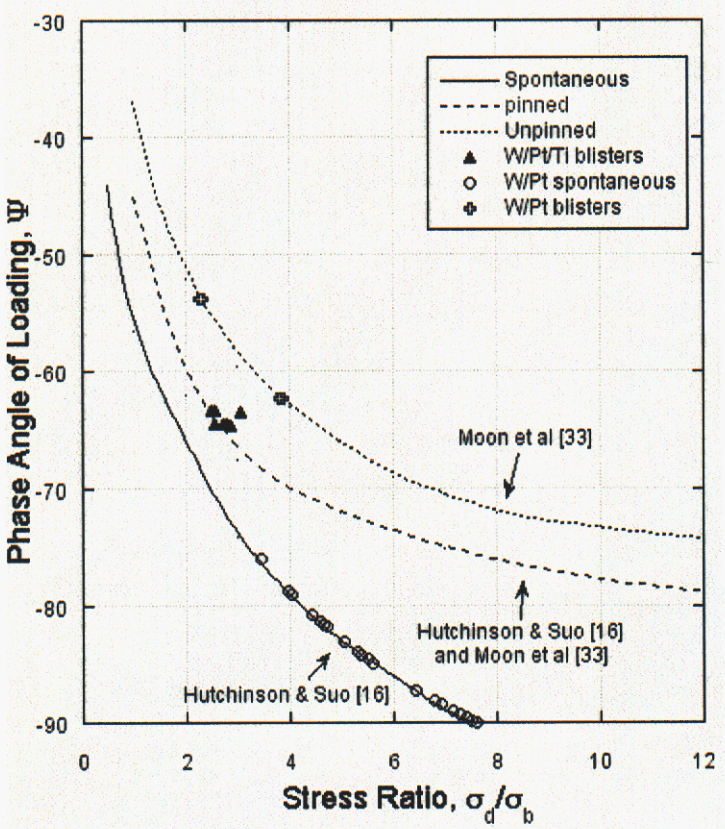

Figure 10: Illustration of how the spontaneous buckles and indentation blisters follow the models of Hutchinson and Suo [16] and Moon et al [33].

2.4 Thin film adhesion conclusions

The interfacial fracture toughness values of the platinum-SiO_2 interface and the titanium-SiO_2 interface have been calculated using both the stressed overlayer method and nanoindentation. Mixed mode adhesion energies, determined from indentation testing, of 0.4 J/m^2 have been calculated for the platinum-SiO_2 interface and 2.0 J/m^2 for the titanium-SiO_2 interface. The mode I interfacial fracture toughness, which is considered the practical work of

adhesion, was calculated to be 0.2 J/m^2 for platinum and 1.0 J/m^2 for titanium, for indentation induced blisters. It has also been shown that the stressed overlayer method is a valid technique to use to quantify the adhesion of thin ductile film interfaces and can be used alone to create spontaneous buckles or in conjunction with nanoindentation to create indentation blisters.

2.5 References

[1] M.D. Kriese, N.R. Moody, and W.W. Gerberich, Acta Materialia **46,** 6623-6630 (1998).

[2] A. A. Volinsky, D. F. Bahr, M. Kriese, N. R. Moody, and W. W. Gerberich, Nanoindentation Methods For Interfacial Fracture Testing, in Encyclopedia on Comprehensive Structural Integrity, vol. 8, Interfacial and Nanoscale Failure, W. W. Gerberich and W. Yang, vol. eds., I. Milne, R. O. Ritchie, B. Karihaloo, editors-in-chief (2003).

[3] A.A. Volinsky, N.R. Moody, and W.W. Gerberich, Acta Materialia. **50,** 441 (2002).

[4] D.S. Rickerby, Surf. Coat. Tech. **36,** 541 (1988).

[5] M.D. Thouless, Eng. Fract. Mech. **61,** 75-81 (1998).

[6] S. Venkataraman, D.L. Kohlstedt, and W.W. Gerberich, J. Mater. Res. **11,** 3133-3145 (1996).

[7] T.W. Wu, J. Mater. Res. **6,** 407-426 (1991).

[8] M.D. Kriese, N.R. Moody, W.W. Gerberich *J. Mater. Res.*, **14** (1999) 3007.

[9] D.B. Marshall and A.G. Evans, J. Appl. Phys **10,** 2632 (1984).

[10] M.P. DeBoer and W.W. Gerberich, Acta. Mater. **44,** 3169-3175 (1996).

[11] M.D. Kriese, N.R. Moody and W.W. Gerberich, J. Mater. Res. **14** 3019 (1999).

[12] L.G Rosenfeld, J.E. Ritter, T.J. Lardner and M.R. Lin, J. Appl. Phys. **67,** 3291-3296 (1990).

[13] R.H. Dauskardt, M. Lane, Q. Ma, N. Krishna, Eng. Fract. Mech. **61**, 141-162 (1998).

[14] A. Bagchi, G.E. Lucas, Z. Suo and A.G. Evans, J. Mater. Res. **9,** 1734-1741 (1994).

[15] A. Bagchi and A.G. Evans, Thin Solid Films **286,** 230-212 (1996).

[16] J.W. Hutchinson and Z. Suo, *Advances in Applied Mechanics* Academic Press, New York, 1992, 64-191.

[17] N.R. Moody, D.P. Adams, M.J. Cordill, N. Yang and D.F. Bahr, Mat. Res. Soc. Symp. Proc. **695,** L7.5.1-6 (2002).

[18] A.A. Volinsky, N.R. Moody and W.W. Gerberich, Mat. Res. Soc. Symp. Proc. **594,** 383-388 (2000).

[19] M.D. Kriese, N.R. Moody and W.W. Gerberich, Mat. Res. Soc. Symp. Proc. **505,** 363-368 (1998).

[20] M.D. Kriese, N.R. Moody and W.W. Gerberich, Acta Mater. **46,** 6623-6630 (1998).

[21] M.Y. He, A.G. Evans and J.W. Hutchinson, Mater. Sci. Eng. **A245,** 168-181 (1998).

[22] N.I. Tymiak, A.A. Volinsky, M.D. Kriese, S.A. Downs and W.W. Gerberich, Metallurgical and Materials Trans A **31A,** 863-872 (2000).

[23] A.G. Evans, J.W. Hutchinson and Y. Wei, Acta Mater. **47,** 4093-4113 (1999).

[24] N.R. Moody, A. Strojny, D.L. Medlin, A. Talin and W.W. Gerberich, J. Mater. Res. **14,** 2306-2313 (1999).

[25] J.A. Schnieder, S.E. Guthrie, M.D. Kriese, W.M. Clift and N.R. Moody, Mater. Sci. Eng. **A259,** 253-260 (1999).

[26] N. Ali, W. Ahmed, C.A. Rego and Q.H. Fan, Diamond and Related Materials **9,** 1464-1420 (2000).

[27] D.L. Polla, L.F. Francis, Ann. Rev. Mat. Sci. **28,** 563-597 (1998).

[28] P. Muralt, J. of Micromechanics and Microengineering **10,** 136-146 (2000).

[29] G. Bernhardt, C. Silvestre, N. LeCursi, S.C. Moulzolf, D.J. Frankel, R.J. Lad, Sensors and Actuators B-Chemical 77, 368-374 (2001).

[30] Z. Suo and J.W. Hutchinson, International Journal of Fracture **43,** 1-18 (1990).

[31] M.D. Thouless, A.G. Evans, M.F. Ashby and J.W. Hutchinson, Acta Metallurgica **35,** 1333-1341 (1987).

[32] M.J. Cordill, N.R. Moody and D.F. Bahr, Mat. Res, Soc. Symp. Proc. **750,** Y.1.8.1-6 (2003).

[33] M.W. Moon, H.M. Jensen, J.W. Hutchinson, K.H. Oh and A.G. Evans, J. Mech Phys Solids **50**, 2355-2377 (2002).

Bulge Testing for Film Fracture

3.1 Bulge testing to fracture

The study of residual stresses in thin films and membranes has become increasingly important in the emerging field of MEMS and high aspect ratio structures because of their effect on system fatigue and fracture. By characterizing and lowering the residual stress within the system, the membrane performance and reliability can be optimized [18]. Interest in both freestanding [19,20,21] and substrate supported films [22] has promoted the use of a variety of testing methods to effectively measure the residual stress. A nondestructive technique that has become popular within the last decade is bulge testing, a method of testing free standing films that is not affected by defects and flaws at the sample edges [3]. The popularity of bulge testing is due to several factors including the ability to measure the residual stress in both single films and composite membranes as well as the variety of film material systems that can be tested, such as ceramics, polymers and metals [1,23]. This method can accurately determine the stresses within micromachined geometric shapes, including round, square, and rectangular membranes. To extrapolate stresses from bulge testing data using developed models [3], accurate material properties such as the elastic modulus and the Poisson's ratio must be known. Although Poisson's ratio does not vary significantly from bulk materials to thin films, it is important to determine the elastic modulus in textured thin film structures. In $Pb(Zr_xTi_{1-x})O_3$ (*X:1-X* PZT) films, the modulus has been reported to range from 54 to 112 GPa [24,25] Coupled with nanoindentation to verify the Young's modulus of the film, the bulge testing method is both accurate and expedient for micromachined structures.

One MEMS device which contains a PZT membrane is the P3 microengine, which utilizes a composite flexing membrane to generate power by converting mechanical energy to electrical energy [26]. Two versions of membrane generator prototypes have been processed. The standard membrane generator processing uses wet etching to create square Si support membranes in Si wafers, after which layers of silicon dioxide, Ti/Pt, PZT, and Au are deposited [27]. Another version, which can potentially provide high aspect ratio devices, uses deep reactive ion etching to create circular membranes with layers of silicon oxide, Ti/Pt PZT and Au over the Si membrane. Characterization and control of the residual stress and processing-structure-property relationships of the PZT is required to optimize both performance and reliability. During operation, these membranes will deform to strains between 0.05 and 0.25%

over several billion cycles. Additionally, to obtain the highest coupling coefficient and electrical output over a given pressure range, no residual stress should be within the membrane when fabrication is complete.

The present study was preformed to characterize the residual stress currently in both of the microengine versions and to quantify the effects of these stresses in each layer with respect to fracture, resonance frequency and electrical properties.

3.2 Bulge testing methods and materials

The PZT films deposited on square membranes (fabricated by wet chemical anisotropic etching) utilized for nanoidentation and bulge testing were composed of 300 nm Au/ 6 nm TiW/1 μm PZT/ 175 nm Pt/ 12 nm Ti/ 1.3 μm Si (where Si is the underlying substrate) and had a side length of 3 mm. Round membranes (formed by deep reactive ion etching) ranged from 1 to 4 mm in diameter and consisted of stacks of 100nm Au/ 1 μm PZT/ 120 nm Pt/ 40 nm Ti/ 1 μm SiO_2. Fabrication procedures of the square and round membranes utilized in this research were previously described [28,29]. Crystallization of the PZT on the square membranes occurred in a furnace at 700°C for 10 min. The PZT on the round membranes was crystallized in air for 60 sec at 700°C using a rapid thermal annealing (RTA) furnace. During processing, wafer curvature was monitored with profilometery using a Tencor FLX-2908. The fabrication of the square membranes used to show the effect of residual stress on the strain was outlined in previous work [30]. A compressively stressed tungsten layer was sputtered onto the pit side of a square 3 mm 40:60 PZT membrane after all other fabrication was completed. This layer was deposited at 2.2 mTorr with 0.35 A. The W layer was thinned using hydrogen peroxide until the residual stress was lowered past the critical buckling criteria.

The Young's modulus values were determined with a Nanoinstruments Nano Indenter II utilizing the continuous stiffness method (CSM) with an AC oscillation of 45 Hz. Indentations were made using a Berkovich Accutip with a nominal root radius of 50 nm. Film thicknesses were determined by either profilometry during fabrication or by cross sectioning the membranes and imaging in a LEO 982 field emission scanning electron microscope (FESEM).

Residual stresses of each membrane were found using pressure-deflection tests and the stress of the PZT was confirmed with x-ray diffraction using a Philips X'Pert MRD Four-Circle

X-ray Diffactometer. During testing, the angle in the plane of the sample between the fixed direction and the projection of the normal diffracting plane, ϕ, was set to 0 and ψ ranged from – 40° to 40° over a 2Θ range of 53 to 58°.

3.3 Bulge testing results

By deforming thin films on small scales using nanoindentation, material properties can easily be measured [31]. Equation 1 shows that the initial unloading stiffness is proportional to the reduced modulus E_r and the square root of the contact area A.

$$S = \frac{dP}{dh} = \frac{2}{\sqrt{\pi}} E_r \sqrt{A} \tag{1}$$

During indentation, the contact stiffness, S, was continuously measured by overlaying a sinusoidal signal of 45 Hz on the load driving the indenter. By analyzing the mechanical response of the system and incorporating equation 1, the elastic modulus of the material can be measured continuously as the tip penetrates into the sample. The elastic modulus extracted from continuous stiffness measurements of the PZT are shown in figure 3.1. Values of the PZT modulus were found by extrapolating the initial linear region of the curve to 0 contact depth, h_c. The PZT films that used rapid thermal annealing of the sol-gel PZT had a modulus of approximately 70 GPa. Both films fabricated using conventional annealing, the 40:60 and 52:48 PZT, showed a modulus of approximately 80 GPa. As the contact depth increases, the modulus values increase towards 160 MPa, the reduced modulus of the Si substrate. These tests were able to determine the modulus while staying in a relatively low strain region, unlike those previously reported by Bahr et al. [32].

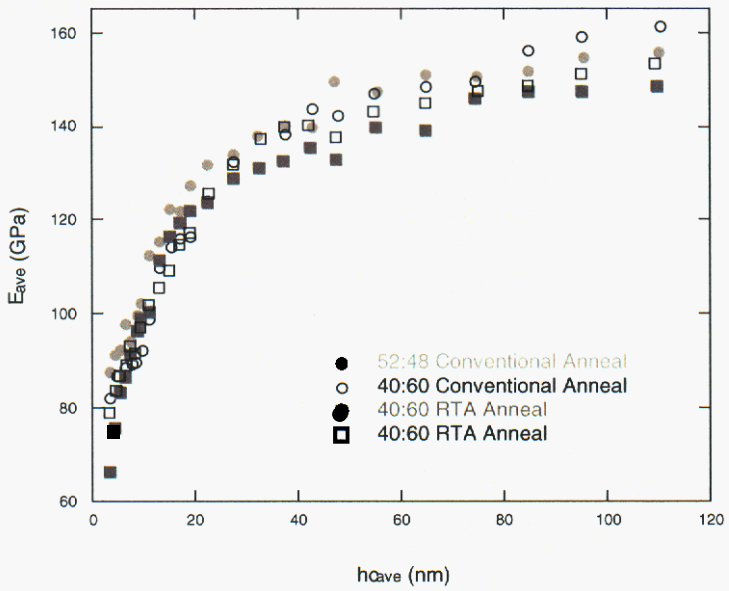

Figure 3.1: CSM nanoindentation of PZT showing the elastic modulus of the various PZT films. The rapid thermal annealed films have a modulus of 70 GPa, conventionally annealed films are 80 GPa.

The stress of the composite membranes was found using static pressure deflection. The relationship between the residual stress, membrane properties and pressure-deflection has been shown to be highly predictable [33,34]. Bonnette et al. showed that the pressure, P, was a function of the deflection W_o, biaxial modulus of the membrane E_B, membrane thickness t, half of the membrane side length a, the residual stress σ_0, and two unitless constants, c_1 and c_2 as shown in equation 2.

$$P(W_o) = \frac{c_1 \sigma_o t W_o}{a^2} + \frac{c_2 E_B t W_o^{\,3}}{a^4} \qquad (2)$$

Assuming the Poisson's ratio of the membrane is 0.25, c_1=3.40 and c_2=1.81 for square membranes and c_1=3.40 and c_2=2.51 for the circular membranes [35]. The biaxial modulus of composite membrane E_c is the weighted average of the individual layers as shown in equation 3 [36] where t_s is the substrate thickness and t_T the total thickness of the membrane.

$$E_c = \frac{t_f}{t_T} E_f + \frac{t_s}{t_T} E_s \qquad (3)$$

Using the thickness values from profilometry and FESEM analysis and the PZT modulus determined by nanoindentation, the biaxial moduli of the RTA and conventional annealed membranes were calculated. The pressure deflection curves for the conventionally annealed membranes are shown in figure 3.2. Fitting the pressure deflection data to equation 2 showed that the stresses vary for both PZT composition and annealing methods. Furnace annealed 52:48 and 40:60 PZT had composite residual tensile stresses of 151 MPa and 101 MPa respectively. RTA annealed 52:48 PZT had a composite residual tensile stress of 154 and 172 MPa.

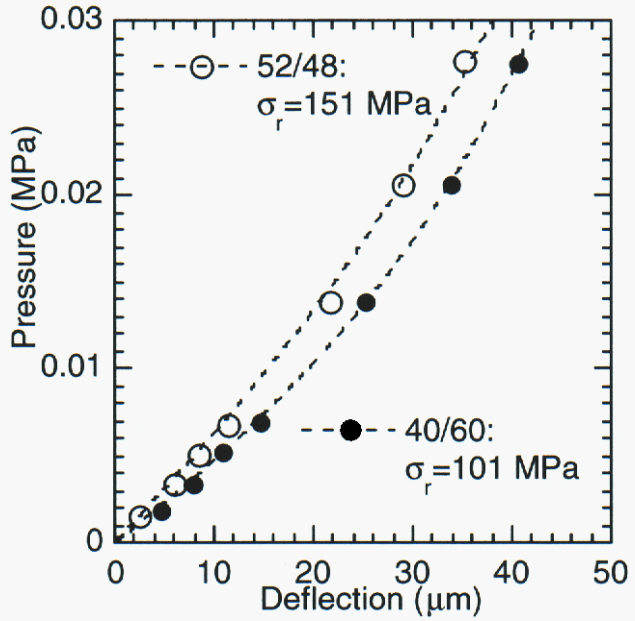

Figure 3.2: Pressure deflection of membranes containing 52:48 and 40:60 PZT films that were conventionally annealed. The membrane residual stress, σ_m, increases as the PZT chemistry changes from 40:60 to 52:48 as indicated by the increased slope.

The wafer curvature was used to calculate residual stresses using Stoney's equation, where the radius of curvature R, initial substrate radius curvature, R_0, substrate thickness T, film thickness t, substrate's elastic modulus E and Poisson's ratio ν yield the magnitude and direction of the residual stress σ [37].

$$\sigma = \frac{1}{(R - R_0)}\left[\frac{E}{(1-\nu)}\right]\left(\frac{T^2}{6t}\right) \qquad (4)$$

Analysis of wafer curvature measurements showed that the layers with the highest stress within the piezoelectric stack were both the Pt bottom electrode after annealing and the PZT. The Pt in the RTA membranes had residual stress of approximately 800 MPa, while the Pt in the conventionally annealed membranes had was around 700 MPa in the tensile direction. These stresses are similar to those seen in the literature; Zakar et al. reported a Pt residual stress of 858 MPa [12] after annealing the Pt bottom electrode at 700°C and Spierings et al. reported after annealing at 500°C the stress of Pt electrode is approximately 1 GPa [38]. At these stresses, plastic flow in the Pt electrodes has been observed [16], which can complicate the stress measurements in other layers.

To quantitatively determine the stress of an individual layer, x-ray diffraction was utilized. This method was used to determine the stress of the PZT since profilometry measurements showed a large stress within this layer. In addition, the PZT comprised a large portion of the effective membrane residual stress due to its thickness. Using this test, the residual stress was examined by measuring the change in planar spacing within the PZT crystals. The residual stress was calculated using equation 5 where the residual stress from a chosen direction of the interplanar spacings, σ_ϕ, is a function of the initial interplanar spacing, d_0, the angle between the normal of the sample ψ, and the measured interplanar spacing d. This method assumes that the angle between the normal of the sample and the normal of the diffracting plane is 0.

$$\sigma_\phi = \frac{E}{(1+\nu)\sin\psi}\frac{(d-d_0)}{d_0} \tag{5}$$

Results from this test are shown in figure 3.3 where the stress in the conventionally annealed 52:48 PZT is higher, 400 MPa, than the conventionally annealed 40:60 PZT, 190 MPa. These stresses are smaller than those calculated for thermal mismatch of the PZT and substrate at room temperature. This stress relaxation has been noted in other works [39].

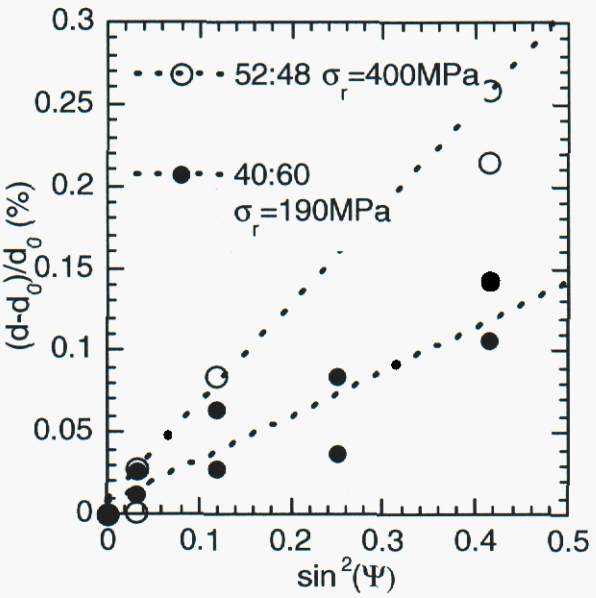

Figure 3.3: The slope of the plot Δd vs. $\sin^2\psi$ is proportional to the stress of the PZT films.

The variation of residual stress affects many aspects of generator performance including compliance, strain at failure and resonance frequency. The applied strain at failure depends upon the amplitude of residual stress, as shown in figure 3.4, where increasing the magnitude of the residual stress decreased the strain at failure of the membranes. This decrease can be rationalized with the theory of a maximum sum of the residual and applied strains to failure.

Since the total stress of the membrane is a weighted average, the residual stress of the composite membrane can be controlled through management of the individual layer stresses. By adding a compressive W layer to the tensile membrane generator, the total composite stress was lowered, as shown in figure 3.5. This additional layer resulted in an increased compliance of 7% and a decrease in resonance frequency from 23 to 18 kHz. These results show the stress can now be controlled by selective usage of compressive layers to balance the highly tensile piezoelectric and electrode thin films.

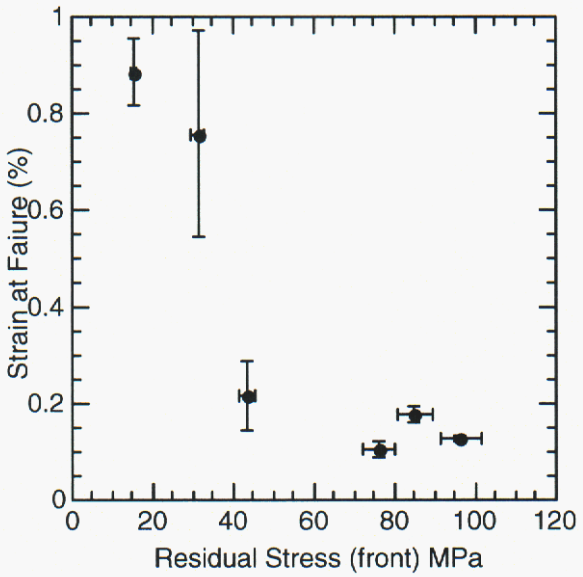

Figure 3.4: There is a strong dependence the applied strain at failure (%) on the residual stress of the membrane. The strain produced is a function of both the applied and residual stresses.

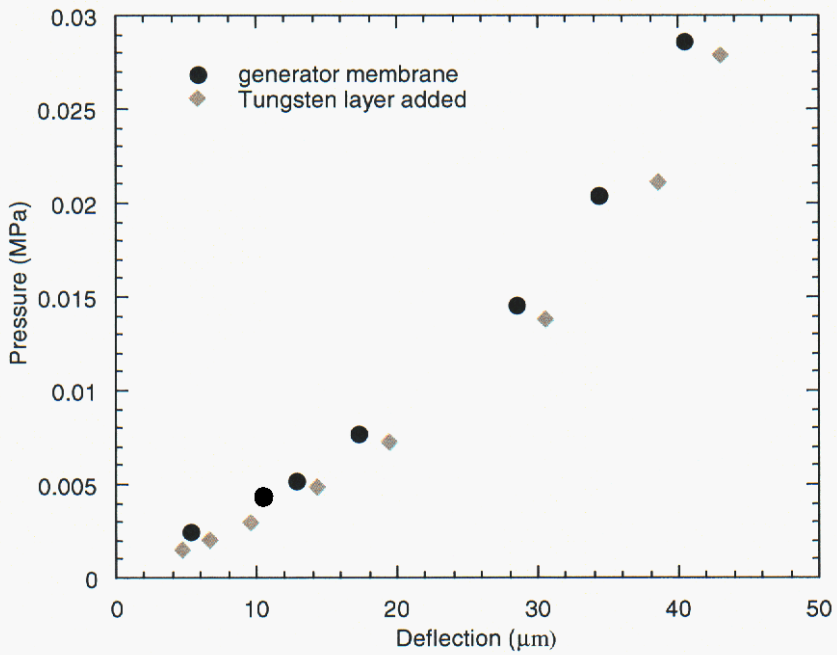

Figure 3.5: The compliance of a microgenerator increases with the decrease of the residual stress. By adding a compressive W underlayer to the tensile microgenerator, the stresses act against each other.

3.4 Bulge testing conclusions

Nanoindentation coupled with the continuous stiffness method allowed for accurate and consistent measurement of the elastic modulus of different compositions and processing variations in 1 μm thick PZT films. Conventionally annealed 52:48 PZT and 40:60 PZT had an elastic modulus of approximately 80 GPa while the RTA annealed 52:48 PZT had a modulus of 70 GPa. These moduli were used to then determine the membrane stress with bulge testing, x-ray diffraction and profilometery experiments. Composite membranes with 1 μm 52:48 PZT had an effective tensile residual stress of 151 MPa reflecting the PZT's high residual stress of 400 MPa. The slowly annealed 40:60 PZT had an effective stress of 101 MPa and PZT film stress of 190 MPa. Residual stresses of the composite membranes were shown to affect the membrane compliance, strain at failure and resonance frequency. In order to counterbalance the membrane tensile stress, a compressively stresses W underlayer was introduced to the membrane. The membrane compliance increased by 7% with the addition of a compressive W underlayer, with a decreasing effective residual stress. This decrease of residual stress resulted in a decrease of resonance frequency from 23 kHz to 18 kHz. These results have shown that the multilayer composite membrane stresses can be tailored to minimize total membrane stress and optimize properties for applications in high aspect ratio structures.

3.5 References

18. Zakar E, Dubey M, Polcawich R, Piekarski B, Piekarz R, Conrad J, Widuta R (2002) Study of PZT film stress in multilayer structures for MEMS devices. Mat Res Soc Symp Proc 605: 287-292

19. Xiang Y, Chen X, Vlassak JJ (2002) The mechanical properties of electroplated Cu thin films measured by means of bulge test technique. Mat Res Soc Symp Proc 695: 189-194

20. Paviot VM, Vlassak JJ, Nix WD (1995) Measuring the mechanical properties of thin metal films by means of bulge testing of micromachined windows. Mat Res Soc Symp Proc 356: 579-584

21. Cieslar M, Karimi A, Martin J-L (2002) Bulge test characterization of static softening and dynamic instabilities in foils of an Al-based alloy. Mat Res Soc Symp Proc 695: 127-132

22. Sengupta SS, Park AM, Payne DA (1997) Integrates electroceramics: densification and stress development in sol-gel derived thin films. Integrated Ferroelelectrics 14: 193-200

23. Nakladal A, Buchhold P, Kohler R, Gerlach G, Stavrev M, Wenzel C, Baumann K, Nowak B (1998) Bulge test investigation of the influence of moisture on mechanical properties of thin polymer layers. Mat Res Soc Symp Proc 518: 105-110

24 . Yu S, K Yao, FTE Hock (2003) Effects of poly(ethylene glycol) additive molecular weight on the microstructure and properties of sol-gel-derived lead zirconate titanate thin films. J Mater Res 10: 737-741

25 . Walter V, P Delobelle, P Le Moal, E Joseph, M Collet (2002) A piezo-mechanical characterization of PZT thick films screen-printed on alumina substrate. Sensors &Actuators: A. physical 96: 157-166

26 . Whalen S, Thompson M, Bahr D, Richards C, Richards R (2003) Design fabrication and testing of the P3 micro heat engine. Sensors & Actuators: A. Physical 104: 200-208

27. Olson BW, Randall LM, Richards CD, Richards RF, Bahr DF (2001) Relationships between microstructure and reliability in PZT MEMS. Mat Res Soc Symp Proc 666: F611-F619

28. Kennedy MS, Bahr DF, Richards CD, Richards RF (2003) Residual stress control to optimize PZT MEMS performance. Mat Res Soc Symp 741: J5.37.1-J5.37.6

29. Zakar E, Polcawich R, Dubey M, Pulskamp J, Piekarski B, Conrad J, Piekarz R (2000) Stress analysis of SiO_2/Ta/Pt/PZT/Pt stacks for MEMS application. IEEE Int Symp App of Ferroelectrics 2: 757-759

30. Olson AL, Skinner JL, Bahr DF, Richards CD, Richards RF (2003) Fracture behavior of thin film PZT on silicon MEMS and membranes. Mat Res Soc Symp 750: Y8.27.1-Y8.27.6

31. Pharr GM, Oliver WC (1992) An improved technique for determining hardness and elastic modulus using load and displacement sensing indentation experiments J. Mater. Res. 7: 1564-1563

32. Bahr DF, Robach JS, Wright JS, Francis LF, Gerberich WW (1999) Mechanical deformation of PZT thin films for MEMS applications. Mat Sci & Eng A259: 126-131

33. Bonnotte E, Delobelle P, Bornier L (1997) Two interferometric methods for the mechanical characterization of thin films by bulge testing tests application to single crystal of silicon. J. Mater. Res. 12: 2234-2248

34. Vlassak, JJ, Nix WD (1992) A new bulge test technique for the determination of young's modulus and poisson's ratio of thin films. J Mat Res **7**: 3242-3249

35. M Small, Vlassak J, Powell S (1993) Accuracy and reliability of bulge testing experiments. Mat Res Symp 308:159-164

36. Shojaei OR, Karimi A (1998) Mechanical properties of TiN thin films measured using nanoindentation and bulge test. Mat Res Symp Proc 522: 245-250

37. Stoney GG (1909) The tension of metallic films deposited by electrolysis. Proc R Soc London Ser A82:172-175

38. Spierings GACM, Dormans GJM, Moors WGJ, Ulenaers MJE, Larson PK (1995) Stresses in Pt/Pb(Zr,Ti)O_3/Pt thin-films stacks for integrates ferroelectric capacitors. J Appl Phys 78: 1926-1933

39. Zhao MH, R Fu, D Lu, TY Lang (2002) Critical cracking of Pb($Zr_{0.53}$ $Ti_{0.47}$)O_3 thin films deposited on Pt/Ti/Si(100) substrates. Acta Mater 50: 4241-4254

Deformation Around Indentations: Dislocation Patterns

4.1 Deformation around indentations: Dislocation Structures

The importance of imaging and examining indentations after they are made is often underestimated. While there certainly is valuable data contained in load depth curves, there is also much information contained in the plastically deformed region around the indentation [40]. Specifically, information about the dislocation mechanisms responsible for deformation can be obtained by examining atomic force microscopy (AFM) images of the slip steps which develop on the surface.

Several studies have been performed on the structure of residual impressions in the literature. Kadijk et al [41] has performed indentations in MnZn ferrite single crystals using spherical tips and identified slip systems responsible for the patterns which resulted in the residual depression. Using a combination or controlled etch pitting, chemo mechanical polishing and AFM, Gaillard et al [42] has described dislocation structures beneath indentations in MgO single crystals. This paper will extend these ideas to a method for identify slip systems in FCC polycrystalline engineering alloys. Other work has been performed on BCC materials to identify changes in surface topography with crystal orientation [43] as well as TEM images of the sub-surface dislocation structure [44].

The FCC crystal structure contains only four unique slip planes. Chang et al [45] describes a method for determining the surface orientation of a particular grain in an FCC material by measuring the angles of the slip step lines on the surface around indentations and calculating the orientation from the combination of angles. With current availability of orientation imaging microscopy (OIM), it is possible to do a similar process in reverse and use the known orientation of a grain to determine the slip plane responsible for each slip step. Each slip plane can be indexed with respect to a reference direction taken from the OIM.

This paper will present an investigation and analysis of the slip step pattern formed around indentations in FCC materials. In addition to identifying the slip systems in these polycrystalline alloys, the character of the slip behavior (wavy versus planar glide) will be demonstrated. This technique should prove useful for correlating indentation hardness values with more macroscopic stress – strain data.

4.2 Deformation testing methods and materials

Ni200, a 99.5% commercially pure Ni alloy, and an austenitic stainless steel were selected as FCC alloys with very different stacking fault energies (SFE). The stainless steel used is a nitrogen strengthened alloy containing 19.1% Cr (by weight), 6.9% Ni, 9.5% Mn, 0.034 C, 0.51 Si and 0.26% N with the balance being Fe. This alloy is commonly referred to simply as 21-6-9 in reference to its nominal compositions of Cr, Ni, and Mn, respectively. Both specimens were annealed at 1200°C for 5 hours and water quenched to produce a large, equiaxed grain structure, with many grains in each specimen measuring up to one millimeter in diameter. OIM grain maps were produced for each sample using a Camscan SEM with a TSL OIM system to reveal the exact orientation of each grain examined. Vickers indentations of 10 to 50 gram loads were placed in grains of various orientations. The indentations were placed away from boundaries in the large grains allowing the local region to be considered as a single crystal. The indentations were imaged using a Park Autoprobe CP AFM in contact mode. Most AFM images shown in this paper are deflection images. As opposed to topography images which map surface height, deflection images map changes in slope. This will accentuate fine details such as slip steps. Additional OIM analysis was conducted to verify the indentations were made in the intended grains.

4.3 Results of dislocation structures around indentations

There are two observations which are noted from the AFM images of slip steps around indentations. The first is the character of individual slip steps and the second is the overall pattern produced by all of the slip steps. The character of the slip steps (a qualitative description of the planar nature of the resulting deformation surrounding the impression) reveals information about the slip mode of the specific material. Figure 4.1 demonstrates the different slip modes present in Ni and 21-6-9 stainless steel. The slip steps in the 21-6-9 are thinner and straighter than those in the Ni. This suggests that planar slip is present in the 21-6-9 and wavy slip in the Ni. These results were predicted based on the stacking fault energy (SFE) of the two metals. Meyers and Chawla [46] report the SFE of Ni to be 128mJ/m^2 whereas the SFE for 21-6-9 has been reported by Schramm [47] to be between 41 and 65 mJ/m^2. Exact values of SFE are difficult to obtain and often vary with the testing method, however the SFE of Ni is inarguably higher than that of 21-6-9.

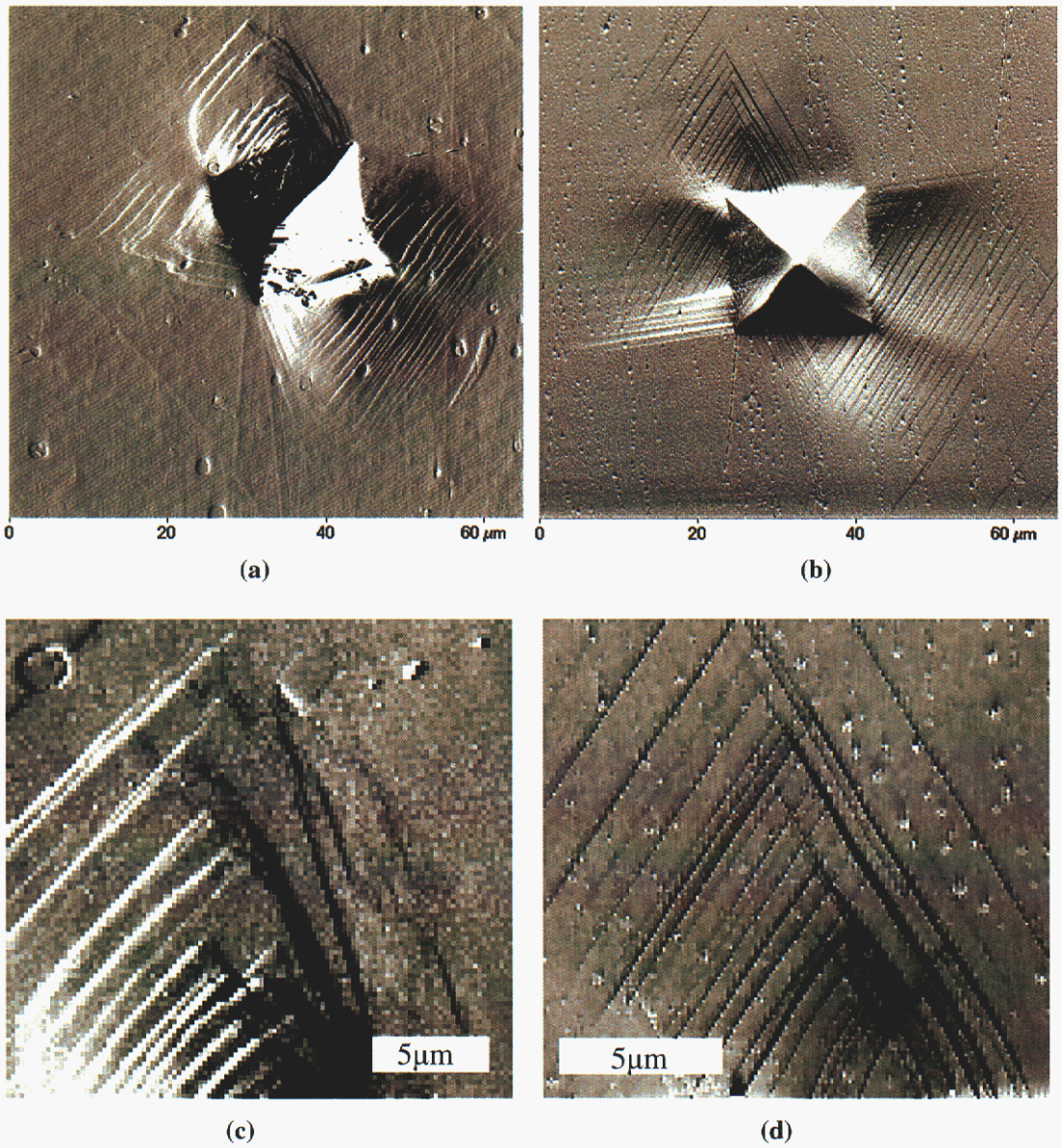

Figure 4.1 Indentations in {110} type grains of Ni (a and c) and 21-6-9 stainless steel (b and d) demonstrate different slip modes are apparent from the thicker and wavier slip lines in the Ni and the thin, straight slip lines in the stainless steel while retaining similar overall patterns. Enlarged regions of each image from (a) and (b) are shown in (c) and (d) respectively.

The second observation from post indentation AFM images is the overall slip step pattern. The slip steps form a pattern on the surface surrounding the impression which varies with the crystal orientation of the surface in which the indentation was made. These patterns are

very repeatable for indentations within the same grain or different grains with the same or similar orientation. Figure 4.2 shows typical slip step patterns in 21-6-9 for orientations close to (001), (011) and (111). Slip patterns from similar grain orientations in different materials also remain similar. Figure 4.1 shows the slip patterns for grains close to (110) type orientations in both Ni and 21-6-9. While the character of the steps is different, the overall patterns are relatively unchanged between the two. 45° axial rotations of the Vickers indenter tip did not significantly affect the overall pattern in any of the grains tested, however localized changes were evident near the corners of the indentation. Some details of these patterns are expected to change with different tip shapes, however, since they are constrained to the available slip planes the basic pattern will not be significantly affected.

The slip step patterns can be used to better understand the dislocation mechanisms taking place beneath the surface. The two indentations shown in Figure 4.3 are from grains close to (001) in 21-6-9 and Ni. Examination of the slip step patterns reveals similar phenomena occurring in both materials. It is important to keep in mind that slip steps are the result of dislocations emerging at the free surface, so they will appear along the line direction which corresponds with the intersection of the slip plane and the surface plane. For a perfect {001} type grain, there will be two line directions possible for slip steps. Both the (111) and $(1\bar{1}\bar{1})$ slip planes will intersect the (001) surface along the $[1\bar{1}0]$ directions and the $(\bar{1}11)$ and $(\bar{1}\bar{1}1)$ slip planes will both intersect the (001) surface along [110]. This orientation is very symmetrical and each of the four {111} planes has the same orientation with respect to the axis of indentation. Therefore, the resolved shear stress should be equal for all four slip planes and equal amounts of slip would be expected for each slip plane.

A grain with an orientation of (015) in Ni and $(0\bar{1}3)$ in 21-6-9 was selected for a detailed analysis of (001) type grain orientations in each material. Both grains were larger than 1mm in diameter allowing many indentations to be placed in each grain. Representative indentations from each are shown in Figure 4.3. Because these are not exactly (001) there will be four unique lines of intersection with the surface rather than two. Measuring the angle between each slip line and the reference direction provided by OIM allows each slip step to be attributed to a specific corresponding slip plane. What was found that only two of the four slip planes are responsible for most of the slip steps visible on the surface.

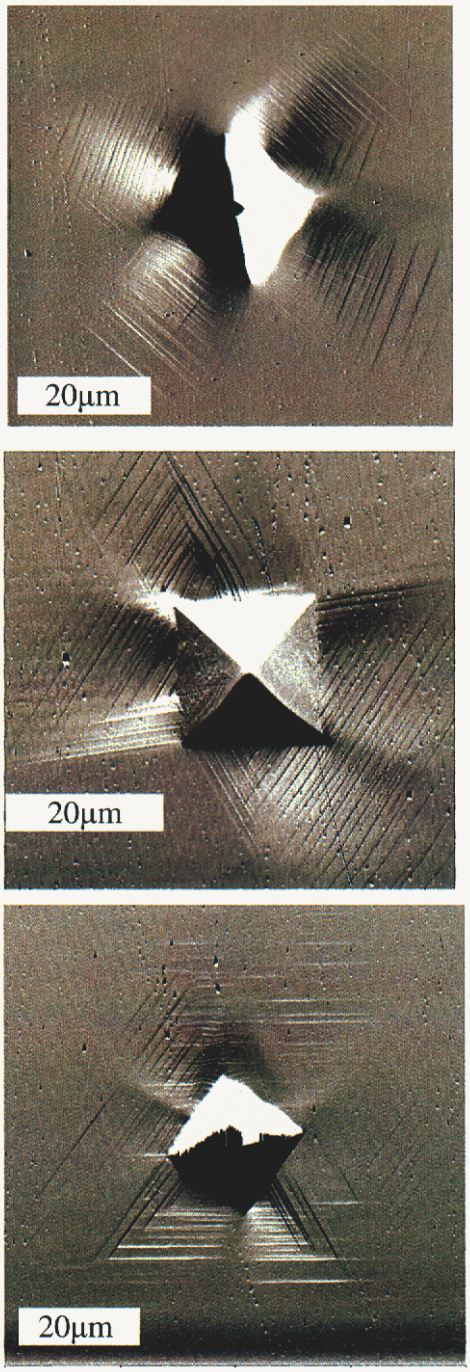

Figure 4.2 Slip steps around indentations form patterns which are dependant on the surface orientation of the grain in which the indentation was made. Shown are AFM images of slip step patterns around indentations in (100) (a) (110) (b) and (111) (c) type grains in 21-6-9 stainless steel.

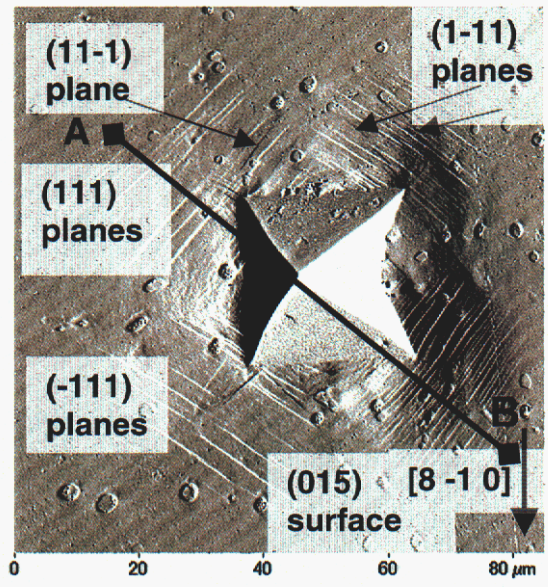

(a)

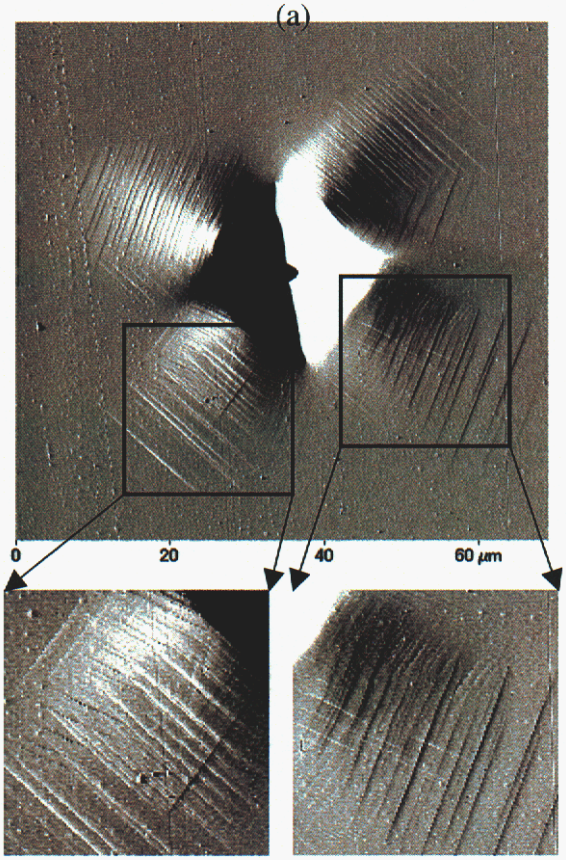

(b)

Figure 4.3 Indentations in (001) type grains of Ni200 (a) and 21-6-9 stainless steel (b) reveal similar slip step patterns. Slip planes are identified in (a) to show that most of the slip steps visible on the surface result from only two of the four possible slip planes. A similar analysis is not labeled on the $(0\bar{1}3)$ grain in 21-6-9 (b) for clarity. The enlarged regions show the faint traces of a second set of slip steps forming at 19.5° to the primary slip steps.

Four lobes of pile up can be observed around each of the indentations in Figure 3. Two of these lobes for each indentation consist of many closely spaced slip steps producing lobes with a higher pile up height. The other two lobes, which are opposite the indentation of each of the other two, consist of larger, coarsely spaced slip steps and produce much lower pile up heights. The slip steps in each opposing set of pile up lobes are parallel indicating that the same slip plane is responsible for all. In both the nickel and the stainless steel, a few slip steps are visible that are not quite parallel. These steps are noted by arrows in Figure 4.3 and the deviation from parallel perfectly matches the deviation expected for each grain orientation. In the case of the (015) nickel grain, this difference is 11.5 degrees and for the $(0\bar{1}3)$ stainless steel it is 19.5 degrees. The presence of these steps greatly increase the confidence that the parallel steps are in fact due to the same parallel set slip planes.

In addition, deflection mode AFM images accentuate features of different slope, so it can be seen that for each pair of pile up lobes (one with fine step spacing and the other, opposite of the indentation, and with coarse spacing) all the steps emerge from the surface with the same step orientation. Figure 4.4 shows a schematic cross section along the line AB from Figure 4.3(a). This figure demonstrates the parallel orientation of the slip planes responsible for the slip steps on either side of the indentation as well as the difference in pile-up heights and the orientation of the steps. Figures 4.4(b) and (c) are actual cross sections taken from the indentation shown in figure 4.3(a).

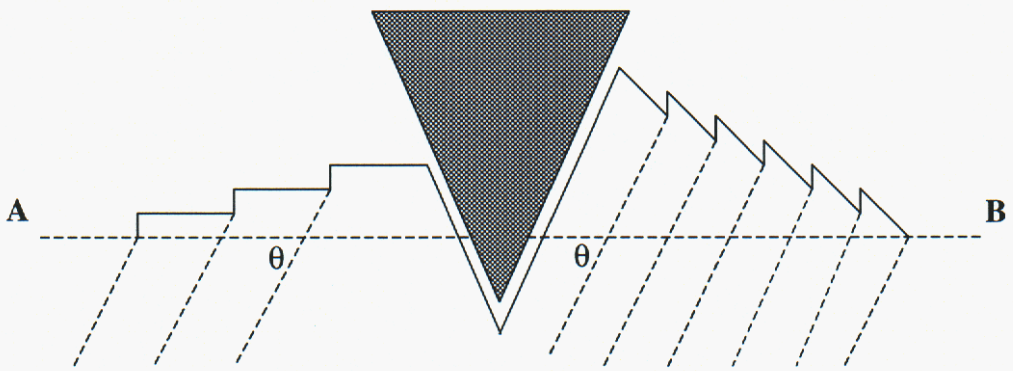

(a)

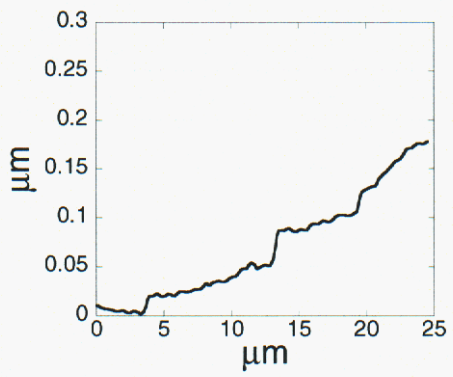

(b)

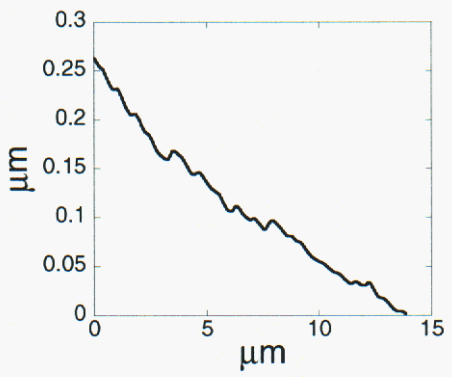

(c)

Figure 4.4 (a)This schematic representation of the cross-section AB from Fig. 3 (a) shows that the slip steps are not symmetrical on either side of the indentation. When moving from A towards B, all the steps are stepping "up." In addition, the steps all appear to be resulting from parallel slip planes beneath the surface. The relative difference in pile-up height between the two sides is also represented. Segments from both sides of the actual AFM cross section are shown in (b) and (c).

4.4 Dislocation pattern conclusions

Indentation testing, combined with AFM and OIM, can be used to the identify slip planes on which dislocations emerge at the free surface around indentations. Patterns of slip steps form around indentations which are very predictable and repeatable. For the FCC materials tested, these patterns appear to be dependant mostly on the crystal orientation. Stacking fault energy and slip mode affects the planarity of any given step.

The slip step patterns around each indentation were extremely repeatable within a single grain and within multiple grains of similar orientation. The patterns also remained very similar for grains of the same orientation in the Ni and the stainless steel. Indentations with the tip rotated by 45 degrees resulted in minor changes near the corners of the tip where the local strain field changes, but the overall pattern remained unchanged

Changes in the slip mode, which is affected by the stacking fault energy, can easily be observed in the character of the slip steps. Slip steps in the stainless steel are very fine and straight whereas those in the nickel are broader and curved. These properties reflect the expectations for planar and wavy glide, respectively.

4.5 References

40. Page TF, Hainsworth SV. Surf. Coating Technol 1993; 61: 201.

41. Kadijk SE, Broese van Groenou A. Acta Metall 1989; 37: 2625.

42. Gailard Y, Tromas C, and Woirgard J. Acta Mater 2003; 51: 1059

43 Stelmashenko NA, Walls MG, Brown LM and Milman Yu V. Acta Metall Mater 1993; 41: 2855.

44 . Zielinski W, Huang H, Venkataraman S and Gerberich WW. Phil. Mag. A 1995; 72: 1221.

45. Chang SC and Chen HC. Acta Metall Mater 1995; 43: 2501.

46. Meyers MA and Chawla KK, Mechanical Metallurgy. Englewood Cliffs, NJ: Prentice Hall; 1984 p. 365.

47. Schramm RE, Reed RP. Met. Trans. A 1975; 6A: 1345.

5. 0 Acknowledgements

This work would not have been possible without the extensive efforts of many students at Washington State University. In particular, we wish to thank:

Bachelor of Science

Mr. Austin Mudd, BS MSE (Dec. 2003)

Mr. Philip Hayenga, BS ME (May 2003)

Master of Science: Materials Science and Engineering

Ms. Christy Woodcock, MS Materials Science and Engineering " Plastic Deformation in Novel Nanoindentation Experiments" (May 2002)

Ms. Megan Jo Cordill, MS Materials Science and Engineering "Adhesion of Thin Ductile Films using Stressed Overlayers and Nanoindentation" (May 2003)

Ms. Marian S. Kennedy, MS Materials Science and Engineering "Residual Stresses and Fracture in Thin Films" (Dec. 2003)

Ph.D. Materials Science

Mr. Kevin Nibur, Ph.D. Materials Science "Localized Deformation Around Indentations" (Dec. 2004)

Appendix

List of Publications and Presentations and Professional Activities under PECASE Award 2000-2003

Journal Publications:

1 *Thin Film Fracture During Nanoindnetation Of A Titanium Oxide Film – Titanium System*
M. Pang and D.F. Bahr, Journal of Materials Research, vol. 16, pp. 2634-2643 (2001)

2 *Thin Film Fracture During Nanoindnetation Of A Titanium Oxide Film – Titanium System*
M. Pang and D.F. Bahr, Journal of Materials Research, vol. 16, pp. 2634-2643 (2001)

3 *Hydrogen and Deformation: Nano- and Microindentation Studies*
D.F. Bahr, K.A. Nibur, K.R. Morasch, and D.P. Field, JOM, vol. 55, no. 2, pp. 27-50 (2003)

4 *Indentation Induced Film Fracture in Hard Film – Soft Substrate Systems*
D.F. Bahr, C.L. Woodcock, M. Pang, K.D. Weaver, and N.R. Moody, International Journal of Fracture, vol. 119, pp. 339-349 (2003)

5 *Identifying slip systems around indentations in FCC metals*
K.A. Nibur and D.F. Bahr, Scripta Materialia, vol. 49, pp. 1055-1060 (2003).

Conference Proceedings:

1 *Film Fracture Phenomena During Indentation*
D.F. Bahr, M. Pang, and D. Rodriguez-Marek, Proceedings of the Materials Research Society, Fundamentals of Nanoindentation and Nanotribology II, eds. S.P. Baker, R.F. Cook, S.G. Corcoran, and N.R. Moody, vol. 649, pp. Q4.2.1 – 4.2.6 (2001)

2 *Plastic Zone Development Around Nanoindentations*
C.L. Woodcock, D.F. Bahr, and N.R. Moody, Proceedings of the Materials Research Society, Fundamentals of Nanoindentation and Nanotribology II, eds. S.P. Baker, R.F. Cook, S.G. Corcoran, and N.R. Moody, vol. 649, pp. Q7.14.1 – 7.14.6 (2001)

3 *Nanoindentation and Orientation Imaging: Probing small volumes and thin films for mechanical properties,* D.F. Bahr, K.A. Nibur and K.R. Morasch, Journal of Electronic Materials, vol. 31, pp. 66 - 70 (2002)

4 *Thin Film Fracture During Nanoindentation Of Hard Film – Soft Substrate Systems,* D.F. Bahr, K.D.Weaver, and D.F. Bahr, Proceedings of the Materials Research, Thin Films Stresses and Mechanical Properties IX, vol. 695, pp. L7.2.1-6 (2002)

5 *Strain Hardening and Cross Slip Measurements From Nanoindentation Experiments,* D.F. Bahr, K.A. Nibur, and M. Pang, in Plasticity, Damage, and Fracture at Macro, Micro, and Nano Scales, ed. Akhtar S. Kahn and Oscar Lopez-Pamies, NEAT PRESS, MD, pp. 60-62 (2002)

6 *Adhesion of Thin Ductile Tilms Using the Stressed Overlayer Method*
M.J. Cordill, N.R. Moody, and D. F. Bahr, in Surface Engineering: In Materials Science II, ed. S. Seal, N.B. Hahortre, J. Moore, S. Suryanarayana, and A. Agarwal, TMS, Warrendale PA, pp. 41-47 (2003)

7 *Localized Deformation Around Nanoindentations and the Effects of Hydrogen on Dislocation Cross Slip*
K.A. Nibur and D.F. Bahr, in Materials Lifetime Science and Engineering, ed. P.K. Liaw, R.A. Buchanan, D.G. Harlow, D.L. Klarstrom, P.F. Tortorelli, and R.P. Wei, TMS, Warrendale PA, pp. 69-75 (2003)

8 *Grain Size Effects on the Adhesion of Thin Ductile Films*
M.J. Cordill, T. Muppidi, and D.F. Bahr, in Proceedings of the Materials Research Society, Mechanical Properties Derived From Nanostructuring (in press 2003)

9 *Indentation Techniques for the Study of Deformation Across Grain Boundaries*
K.A. Nibur and D.F. Bahr, in Proceedings of the Materials Research Society, Mechanical Properties Derived From Nanostructuring (in press 2003)

Student Thesis at Washington State University:

Ms. Christy Woodcock, Materials Science and Engineering " Plastic Deformation in Novel Nanoindentation Experiments" (May 2002)

Ms. Megan Jo Cordill, Materials Science and Engineering "Adhesion of Thin Ductile Films using Stressed Overlayers and Nanoindentation" (May 2003)

Presentations:

1 *Film Fracture Controlled Excursions in Oxide-Metal Systems*
D.F. Bahr, M. Pang, and D. Rodriguez-Marek, Materials Research Society Fall Meeting, Symposium Q, Fundamentals of Nanoindentation and Nanotribology II (Nov. 27-Dec. 1, 2000)

2 *Plastic Zone Development Around Nanoindentations*
C.L. Woodcock, D.F. Bahr, and N.R. Moody, Materials Research Society Fall Meeting, Symposium Q, Fundamentals of Nanoindentation and Nanotribology II (Nov. 27-Dec. 1, 2000)

3 *Slip Band and Step Formation Around Small Scale Indentations*
D.F. Bahr, C.L. Woodcock, and K.R. Morasch, Materials Research Society Spring Meeting, Symposium BB, Material Instabilities and Patterning in Metals (April 16-20, 2001)

4 *Passive Film Fracture in Corrosive Environments,* D.F. Bahr, Pacific Northwest National Laboratories, Stress Corrosion Cracking Technical Seminar, September 7, Richland, WA (2001)

5 *Thin Film Fracture During Nanoindentation Of Hard Film – Soft Substrate Systems,*D.F. Bahr, K.D.Weaver, and D.F. Bahr, Materials Research Society Fall Meeting, Symposium L, Thin Films Stresses and Mechanical Properties IX, Boston, MA (December 2001)

6 *Deformation and Fracture in Metal Oxide Multilayers using Nanoindentation,* Christy L. Woodcock and D.F. Bahr, Deformation and Stresses in Small Volumes Symposium, TMS 2002 Annual Meeting, Seattle, WA (Feb.2002)

7 *Probing Hydrogen – Deformation Interactions Using Nanoindentation*
D.F. Bahr, K.A. Nibur, K.A. Morasch, and D.P. Field, International Conference on Hydrogen Effects on Material Behavior and Corrosion Deformation Interactions, September 23 (2002).

8 *Adhesion of Thin Ductile Tilms Using the Stressed Overlayer Method*
M.J. Cordill, N.R. Moody, and D. F. Bahr, Surface Engineering: In Materials Science II, TMS 2003 Annual Meeting, San Diego, CA (March 2003)

9 *Localized Deformation Around Nanoindentations and the Effects of Hydrogen on Dislocation Cross Slip*
K.A. Nibur and D.F. Bahr, iMaterials Lifetime Science and Engineering, TMS 2003 Annual Meeting, San Diego, CA (March 2003)

10 *Grain Size Effects on the Adhesion of Thin Ductile Films*
M.J. Cordill, T. Muppidi, and D.F. Bahr, Materials Research Society Spring Meeting, Mechanical Properties Derived From Nanostructuring Symposium (April 2003)

11 *Indentation Techniques for the Study of Deformation Across Grain Boundaries*
K.A. Nibur and D.F. Bahr, Materials Research Society Spring Meeting, Mechanical Properties Derived From Nanostructuring Symposium (April 2003)

Professional Activities:

Session chair for Materials Research Society Fall Meeting, Symposium Q, Fundamentals of Nanoindentation and Nanotribology II (Dec. 2000)

Session chair for Materials Research Society Spring Meeting, Symposium BB, Material Instabilities and Patterning in Metals (April 2001)

Symposium Organizer (with N.R. Moody) for "Deformation and Stresses in Small Volumes", TMS 2002 Annual Meeting, Seattle, WA (Feb. 2002).

Symposium Organizer (with N.R. Moody) for "Mechanical Properties Derived From Nanotructuring", Materials Research Society Spring Meeting (April 2003)

Distribution

1	MS 0889	B. L. Boyce, 1851
1	MS 0889	T. E. Buchheit, 1851
1	MS 0889	J. W. Braithwaite, 1832
1	MS 0889	S. V. Prasad, 1851
1	MS 0893	D.E. Reedy, 9123
1	MS 0958	J.A.Emerson 14172
1	MS 0958	P J. Cole, 14172
1	MS 0959	D.P. Adams, 14171
1	MS 1310	M. P De Boer, 1762
1	MS 9405	J.M. Hruby, 8700; Attn:
	MS 8751	J.E. Goldsmith, 8751
	MS 8752	C. Moen, 8752
	MS 9409	W.C. Replogle, 8771,
	MS 8773	J Wang, 8773
1	MS 9042	P. A. Spence, 8774
1	MS 9402	C. Cadden,8772
1	MS 9402	S. W. San Marchi 8772
1	MS 9402	N.Y. Yang, 8773
1	MS 9404	G.D. Kubiak, 8750
1	MS 9405	R.E. Jones, 8763
1	MS 9405	D.J. Bammann, 8763
1	MS 9405	E.B.Marin, 8763
1	MS 9405	K. L. Wilson, 8770
1	MS 9409	W.Y. Lu, 8754
1	MS 9409	S. Lee,8754
1	MS 9409	S.H. Goods, 8754
1	MS 9409	S.X. McFadden, 08754
1	MS 9409	J. R. Garcia, 8725
5	MS 9409	N. Moody, 8725
1	MS 9161	W. R. Even, 8760
1	MS 9161	D.L. Medlin, 8761
1	MS 9161	T. Chen, 8763
1	MS9161	K. E. McCarty, 8761
3	MS 9018	Central Technical Files, 8945-1
1	MS 0899	Technical Library, 9616
1	MS 9021	Classification Office, 8511 for Technical Library, MS 0899, 9616 DOE/OSTI via URL
1	MS 0323	D. Chavez, LDRD Office, 1011

This page intentionally left blank